PHYSICAL REVIEW B **93**, 235101 (2016)

Interleaved numerical renormalization group as an efficient multiband impurity solver

K. M. Stadler,[1] A. K. Mitchell,[2] J. von Delft,[1,*] and A. Weichselbaum[1]
[1]*Physics Department, Arnold Sommerfeld Center for Theoretical Physics and Center for NanoScience, Ludwig-Maximilians-Universität München, 80333 München, Germany*
[2]*Institute for Theoretical Physics, Utrecht University, Leuvenlaan 4, 3584 CE Utrecht, The Netherlands*

(Received 12 February 2016; revised manuscript received 24 March 2016; published 1 June 2016)

Quantum impurity problems can be solved using the numerical renormalization group (NRG), which involves discretizing the free conduction electron system and mapping to a "Wilson chain." It was shown recently that Wilson chains for different electronic species can be interleaved by use of a modified discretization, dramatically increasing the numerical efficiency of the RG scheme [Phys. Rev. B **89**, 121105(R) (2014)]. Here we systematically examine the accuracy and efficiency of the "interleaved" NRG (iNRG) method in the context of the single impurity Anderson model, the two-channel Kondo model, and a three-channel Anderson-Hund model. The performance of iNRG is explicitly compared with "standard" NRG (sNRG): when the average number of states kept per iteration is the same in both calculations, the accuracy of iNRG is equivalent to that of sNRG but the computational costs are significantly lower in iNRG when the same symmetries are exploited. Although iNRG weakly breaks SU(N) channel symmetry (if present), both accuracy and numerical cost are entirely competitive with sNRG exploiting full symmetries. iNRG is therefore shown to be a viable and technically simple alternative to sNRG for high-symmetry models. Moreover, iNRG can be used to solve a range of lower-symmetry multiband problems that are inaccessible to sNRG.

DOI: 10.1103/PhysRevB.93.235101

I. INTRODUCTION AND MOTIVATION

Quantum impurity problems are relevant to a range of physical phenomena in which strong electron correlations play a key role [1]. They describe a generic class of systems comprising a few interacting degrees of freedom coupled to a continuum bath of noninteracting conduction electrons. The Kondo model [2] is the simplest exemplar, featuring a single spin-$\frac{1}{2}$ "impurity" coupled to a single spinful conduction electron channel. The basic physics can be understood within the renormalization group (RG) framework: the effective impurity-bath coupling grows as the temperature/energy scale is reduced. The RG flow from weak to strong coupling is characterized by the Kondo temperature T_K, which sets the scale for onset of strong coupling physics and the dynamical screening of the impurity spin by conduction electrons [1].

A detailed understanding of this problem was first obtained using Wilson's numerical renormalization group (NRG) [3–5]. The method involves discretization of the conduction electron Hamiltonian, and mapping to a 1D tight-binding Wilson chain. The transformation is defined so that the interacting impurity subsystem couples to one end of the noninteracting Wilson chain. A special form of the discretization is used that ensures exponential decay of hopping matrix elements down the chain [3]. This energy-scale separation justifies an RG scheme based on successive diagonalization and truncation, starting at the impurity subsystem and working down the chain. At each step, a Wilson shell with d_{loc} additional local quantum degrees of freedom couples into the system, but only the lowest N_{K} eigenstates of the enlarged state space are kept after diagonalization. This scheme ensures that the Fock space of kept states does not increase exponentially with chain length, and allows the physics to be investigated at successively lower energies.

The computational costs of using NRG scale *exponentially* with the number of fermionic bands (distinct flavors), m, involved in the quantum impurity model. The power and applicability of NRG would be greatly improved if these numerical costs could be reduced, since *multiflavor* quantum impurity problems appear in a wide range of contexts. For example, iron impurities in gold are described by a spin-$\frac{3}{2}$ three-channel Kondo model [6,7]; multiple impurities separated in real space [8,9] or manipulated by STM [10] necessitate a multichannel description, as do magnetic nanostructures [11]; single carbon nanotube quantum dots display entangled spin-orbital SU(4) Kondo physics [12], while certain nanotube double dot [13] and multilead semiconductor coupled dot devices [14–16] are described by generalized two-channel models; and nanowire/superconductor heterostructures hosting lead-coupled Majorana fermions give rise to effective multichannel topological Kondo models [17,18]. Furthermore, quantum impurity problems appear as effective local models within dynamical mean-field theory (DMFT) for correlated materials. Multiorbital/band lattice models map to generalized multichannel impurity problems [19–21], and in cluster extensions of DMFT, the number of bands of the effective impurity model scales with the number of cluster sites [22].

There is thus much incentive to improve the efficiency of NRG when dealing with multiflavor models. The present paper aims to make a contribution towards this goal, by offering a detailed analysis of a recently-proposed scheme of "interleaving" the Wilson chains for different fermion flavors [23]. Having a purely methodological focus, it is based on well-studied physical models and is particularly addressed at a readership of NRG practitioners. New physical applications of iNRG are left for follow-up projects.

To set the scene, we first briefly summarize why the numerical costs of NRG scale exponentially with m. For a

---

[*] Corresponding author: vondelft@lmu.de

given conduction electron discretization, the *accuracy* of the calculation is controlled by the number of states *retained* or *kept* at each step of the iterative RG scheme, N_K. On the other hand, the computational *cost* of an NRG run is controlled by the *total size* of the Hilbert space to be diagonalized at each step, $N_\mathrm{tot} = N_\mathrm{K} \times d_\mathrm{loc}$, which is the tensor product of the space of states retained from the previous iteration (of dimension N_K), and the state space of a newly added Wilson shell (of dimension d_loc). The computational time for matrix diagonalization scales as N_tot^3, while the memory required scales as N_tot^2. In Wilson's original "standard" NRG formulation [3] (sNRG), the local dimension for a system with m distinct fermionic flavors scales exponentially in m, $d_\mathrm{loc}^\mathrm{sNRG} = d_\mathrm{f}^m$, with d_f the state space dimension of a single flavor. For a single fermionic level, it follows that $d_\mathrm{f} = 2$, since it can be either occupied or unoccupied. Commonly, quantum impurity models involve N_c channels of *spinful* conduction electrons. In this case, $m = 2N_\mathrm{c}$, such that $d_\mathrm{loc}^\mathrm{sNRG} = 4^{N_\mathrm{c}}$.

In fact, as the number m of flavors increases, the number N_K of states kept at each step of an NRG calculation must also be increased to maintain the same accuracy (i.e., the same degree of numerical convergence). We find that for converged sNRG calculations, N_K scales roughly exponentially with the number of flavors, which we will indicate by writing $N_\mathrm{K} \equiv N_\mathrm{K}^{(m)}$. This scaling property is demonstrated explicitly in this paper.

Overall then, N_tot depends exponentially on m through both N_K and d_loc in sNRG:

$$N_\mathrm{tot}^\mathrm{sNRG} = N_\mathrm{K}^{(m)} \times d_\mathrm{f}^m \ . \tag{1}$$

This exponential scaling imposes severe limitations on the applicability of sNRG to treat quantum impurity problems with several conduction electron channels. In practice, unless large symmetries can be exploited, sNRG cannot be used for problems with more than two spinful channels.

Two approaches have been developed to improve the efficiency of NRG applied to multichannel quantum impurity models. One approach exploits non-Abelian symmetries if present: diagonalization of the NRG Hamiltonian at each step can then be done in *multiplet* space rather than state space, significantly reducing the matrix sizes and hence computational cost.

From the very first sNRG studies of the Anderson impurity model [4], it was essential to exploit the SU(2) spin symmetry so that the calculations could be performed with the limited computational resources available at that time. In Ref. [24], the use of SU(2) symmetries was incorporated into the framework of the density-matrix (DM) NRG [25] to obtain dynamical results for a symmetric two-channel model. Finally, a generalized and flexible framework was pioneered in Ref. [26], which now allows much larger symmetries to be handled, including arbitrary non-Abelian symmetries. The precise gain in computational efficiency with this scheme naturally depends on the specific model and its symmetries; its scope of application is of course limited when symmetry-breaking perturbations (such as a magnetic field) are present.

A second, very different strategy has recently been proposed in Ref. [23]. This "interleaved" NRG (iNRG) method, described in detail in Sec. II, introduces slightly different discretization schemes for conduction bands of different electronic flavors, leading to inequivalent Wilson chains (even for flavors related by symmetries of the bare model). For m electronic flavors, the m Wilson chains are interleaved to form a single generalized Wilson chain [23], which still has the required property of exponential energy-scale separation down the chain. The diagonalization and truncation step in iNRG is then done *separately* after addition of *each* electron flavor, rather than after addition of the entire "shell" of m flavors, as in sNRG. In practice, we specify the truncation threshold not by fixing the number of states to be kept, but by fixing a truncation energy: all states with higher energies are discarded at every step.

Full interleaving leads to a reduction of the local state space from $d_\mathrm{loc}^\mathrm{sNRG} = d_\mathrm{f}^m$ in sNRG to $d_\mathrm{loc}^\mathrm{iNRG} = d_\mathrm{f}$ in iNRG, independent of m. However, it also raises the question as to whether the truncation energy required to reach accurate, well-converged results needs to be changed when switching from sNRG to iNRG. One of the main conclusions of the present paper is that it essentially does not change: an extensive comparison of iNRG and sNRG results, obtained using comparable discretization settings and exploiting the same symmetries for both methods, shows that results of comparable accuracy are obtained if on average the "same" truncation energy is used (see Sec. II C for a detailed discussion). Moreover, this implies that the number of states kept at a given step is the same, on average, for both methods:

$$N_\mathrm{K}^\mathrm{iNRG} \simeq N_\mathrm{K}^\mathrm{sNRG} \equiv N_\mathrm{K}^{(m)} . \tag{2}$$

We find that $N_\mathrm{K}^{(m)}$ still depends exponentially on m, as for sNRG. Thus, for iNRG, the computational costs are governed by

$$N_\mathrm{tot}^\mathrm{iNRG} = N_\mathrm{K}^{(m)} \times d_\mathrm{f} \, , \tag{3}$$

where the first factor $N_\mathrm{K}^{(m)}$ is essentially the same as that in Eq. (1) for $N_\mathrm{tot}^\mathrm{sNRG}$. However, the exponential dependence of d_loc on m in the second factor is entirely eliminated in iNRG.

As a result, when equivalent settings are used for both methods, iNRG yields results of comparable accuracy as sNRG at dramatically reduced numerical cost: computation times are smaller by a factor of order $(N_\mathrm{tot}^\mathrm{sNRG}/N_\mathrm{tot}^\mathrm{iNRG})^3 = d_\mathrm{f}^{3(m-1)}$, and the required storage resources are smaller by a factor of order $d_\mathrm{f}^{2(m-1)}$.

Although d_loc is smaller in iNRG than sNRG, an additional minor cost is incurred in iNRG because the interleaved Wilson chain is m times longer than the standard Wilson chain (resulting in an additional *linear* increase in overall computation time with m). Furthermore, fine tuning of bare parameters is also necessary for effective restoration of broken symmetries in cases where flavor symmetry-breaking is a relevant perturbation, requiring multiple iNRG runs (the exponentially rapid convergence in the number of runs is discussed in Sec. IV E).

The conclusions summarized above are established in this paper by a direct comparison of iNRG and sNRG for several symmetric quantum impurity problems (specified in Sec. III) with $N_\mathrm{c} = 1$, 2, and 3 spinful conduction electron channels. Within iNRG, we explore different ways of interleaving the electronic flavors, and exploit all symmetries that remain after interleaving. For each such iNRG calculation, we perform a corresponding sNRG calculation using the same symmetries, a comparable discretization choice, and the same average truncation energies, i.e., we adopt “equivalent settings.” Moreover, for each model, we also perform a set of benchmark calculations exploiting the *full* symmetries of the bare model, serving as an absolute reference.

Our iNRG-sNRG comparison for equivalent settings focuses particularly on comparing their *efficiency* (Sec. IV C) and their *accuracy* (Sec. IV D). We determine efficiency by tracking representative CPU times. We gauge accuracy in two ways: (i) deviations of numerically computed physical quantities from certain exact results yield an absolute measure of the accuracy of both methods; (ii) the discarded weight [27] estimates the degree of numerical convergence of a given NRG run (see also Sec. II D).

It may be surprising at first that the accuracy of iNRG and sNRG are equivalent when using equivalent settings, since iNRG involves significantly more truncation steps. This result can, however, be rationalized by noting that the truncation at each step of iNRG is less severe than in sNRG (fewer states are discarded at any given step), producing a more fine-grained RG description. For equivalent settings, iNRG clearly outperforms sNRG in terms of efficiency because the state space diagonalized at each step is much smaller in iNRG. In fact, for the high-symmetry multiband models studied here, iNRG is absolutely competitive even when compared to sNRG calculations that exploit the *full* symmetry of the model.

This finding greatly increases the scope of possibilities available for NRG treatments of multiband impurity models. For models with high symmetries, *both* sNRG and iNRG can be highly efficient methods. In such cases, iNRG is a viable and technically simple alternative to sNRG. For models having lower symmetries (for example, when a magnetic field is applied, particle-hole symmetry is broken, or other channel anisotropies are present), iNRG has a clear advantage over sNRG.

In a pure renormalization group (RG) sense, the artificial symmetry breaking, of course, is clearly also visible in the resulting energy flow diagrams derived from finite-size spectra [3–5]. There, a full RG step, which in sNRG requires two iterations (e.g., to get from one even site to the next even site), now requires $2m$ iNRG steps. Nevertheless, aside from possible fine-tuning as discussed in Sec. IV E, this does not affect the energy scales of different phases (fixed points) [23] nor does it affect thermodynamical physical quantities of the model of interest.

II. METHODS

The Hamiltonian of quantum impurity models has the form

$$\hat{H} = \hat{H}_{\text{imp}} + \hat{H}_{\text{cpl}}(\{\hat{f}_{0\nu}\}) + \hat{H}_{\text{bath}} \,. \tag{4}$$

It describes an interacting “impurity” subsystem, $\hat{H}_{\text{imp}}$, coupled by $\hat{H}_{\text{cpl}}(\{\hat{f}_{0\nu}\})$ to a bath of noninteracting conduction electrons,

$$\hat{H}_{\text{bath}} = \sum_{\nu=1}^{m}\sum_{k} \varepsilon_{k\nu}\hat{c}^{\dagger}_{k\nu}\hat{c}_{k\nu}, \tag{5}$$

where $\nu = 1,\ldots,m$ labels the m distinct electron flavors, and $\hat{c}^{\dagger}_{k\nu}$ creates an electron with a given flavor ν and momentum k at energy $\epsilon_{k\nu} \in [-D_\nu, D_\nu]$. The impurity is taken to be located at real-space site $\mathbf{r} = 0$, and coupled to local bath sites $\hat{f}_{0\nu} = V_\nu^{-1}\sum_k V_{k\nu}\hat{c}_{k\nu}$, with the normalization factor $|V_\nu|^2 = \sum_k |V_{k\nu}|^2$. The density of bath states with flavor ν at the impurity position is then given by $\rho_\nu(\omega) = \sum_k |V_{k\nu}/V_\nu|^2\delta(\omega - \epsilon_{k\nu})$, defined inside a band of half-width D_ν. We assume constant (momentum-independent) couplings for which the density of bath states simplifies to a box function, $\rho_\nu(\omega) = \Theta(\omega - |\epsilon|)/(2D_\nu)$. When N_{c} channels of spinful conduction electrons are involved, $\nu \equiv (\alpha,\sigma)$, where $\alpha \in \{1,\ldots,N_{\text{c}}\}$ labels channels and $\sigma \in \{\uparrow, \downarrow\}$ labels spins.

A. Standard Wilson chains

Within sNRG, $\hat{H}_{\text{bath}}$ is discretized and mapped onto a 1D tight-binding Wilson chain [3], consisting of m identical “subchains,” one for each flavor. The subchains are constructed as follows: first, each band $\rho_\nu(\omega)$ is divided up into energy intervals with exponentially reducing width. The discretization points are given by

$$\epsilon^{\pm}_{n\nu}(z) = \begin{cases} \pm D_\nu & n = 0, \\ \pm D_\nu\,\Lambda^{-n+z_\nu} & n = 1,2,\ldots, \end{cases} \tag{6}$$

where $\Lambda > 1$ is a dimensionless discretization parameter, and $z_\nu \in [0,1[$ (defined modulo 1) is a continuous “twist” parameter that shifts the discretization points. Conventionally, the twist parameter is applied symmetrically to all electronic flavors by choosing $z_\nu \equiv z$. If desired, results of N_z separate NRG runs with uniformly distributed z can be averaged to remove certain discretization artifacts [28,29].

A discretized version of the continuous spectrum $\rho_\nu(\omega)$ is obtained by replacing the electron density in each interval by a single pole of the same total weight,

$$\rho^{\text{disc}}_\nu(\omega,z) = \sum_{n=0}^{\infty}\sum_{\lambda=\pm}\gamma^{\lambda}_{n\nu}(z)\delta\big(\omega - \xi^{\lambda}_{n\nu}(z)\big), \tag{7}$$

where $\gamma^{\lambda}_{n\nu}(z) = \int_{\epsilon^{\lambda}_{n+1,\nu}(z)}^{\epsilon^{\lambda}_{n\nu}(z)} d\omega\rho_\nu(\omega)$ gives the pole weights. The pole positions, $\xi^{\lambda}_{n\nu}(z)$, are determined from a differential equation introduced in Ref. [30], which is based on the condition that the original (continuous) bath density of states is reproduced exactly in the limit $N_z \to \infty$ after z averaging, $\rho_\nu(\omega) = \int_0^1 dz\rho^{\text{disc}}_\nu(\omega,z)$. For constant density of states, we use

$$\gamma^{\lambda}_{n\nu}(z) = D_\nu\begin{cases} 1 - \Lambda^{z-1} & n = 0 \\ \big(1 - \frac{1}{\Lambda}\big)\Lambda^{-n+z} & n = 1,2,\ldots \end{cases}, \tag{8a}$$

$$\xi^{\lambda}_{n\nu}(z) = \lambda\frac{\gamma^{\lambda}_{n\nu}(z)}{\ln\Lambda}\begin{cases} +z & n = 0 \\ 1 & n = 1,2,\ldots \end{cases}. \tag{8b}$$

The Wilson subchain for flavor ν is defined uniquely [3] as the semi-infinite 1D tight-binding chain that reproduces the discretized density of states $\rho^{\text{disc}}_\nu(\omega)$ at the terminal site. The discretized bath is represented by the sum of all m Wilson subchains, which together form the “full” Wilson chain, with Hamiltonian

$$\hat{H}^{\text{disc}}_{\text{bath}} = \sum_{\nu=1}^{m}\sum_{n=0}^{\infty}[(t_{n\nu}f^{\dagger}_{n,\nu}f_{n+1,\nu} + \text{H.c.}) + \varepsilon_{n\nu}f^{\dagger}_{n,\nu}f_{n,\nu}], \tag{9}$$

The Wilson chain coefficients $t_{n\nu}$ and $\varepsilon_{n\nu}$ are obtained in practice by Lanczos tridiagonalization [5] [in contrast to the index k in Eq. (5), n refers to sites of the Wilson chain].

Importantly, due to the logarithmic discretization, the hopping matrix elements decay exponentially along each subchain [3],

$$t_{n\nu}/D_\nu \sim \Lambda^{z_\nu - n/2}, \tag{10}$$

for $n \gg 1$, and as such depend on NRG discretization parameters Λ and z_ν. For equal bandwidths $D_\nu \equiv D$ and constant $z_\nu \equiv z$, there is an energy-scale separation between sites with different n,

$$t_{n+1,\nu}/t_{n\nu} \overset{\text{sNRG}}{\sim} \Lambda^{-1/2}\,. \tag{11}$$

However, since the subchains are identical for sNRG, there is no scale separation between different flavors with the same site index n. Together, these flavors form "supersite" n of the full Wilson chain: they all have the *same* characteristic energy scale

$$\omega_n = a\Lambda^{-n/2}\,, \tag{12}$$

(the constant a is chosen such that the rescaled hoppings $t_{n-1}/\omega_n \to 1$ as $n \to \infty$). As a consequence, all m subsites of supersite n must be treated equivalently in a single step in sNRG.

The discretized model Hamiltonian in Eqs. (4) and (9) is diagonalized iteratively [3], starting at the impurity and working down the chain in sNRG by adding an entire supersite at each iteration n. The energy-scale separation embodied by Eq. (11) justifies truncation at each step: the lowest N_K states are kept, forming a Wilson "supershell," and the remaining $N_\mathrm{K}\times(d_\mathrm{f}^m - 1)$ states are discarded. If the eigenenergies E_n of supershell n are given in units of ω_n ("rescaled units"), the typical level spacing of the lowest-lying levels is of order 1.

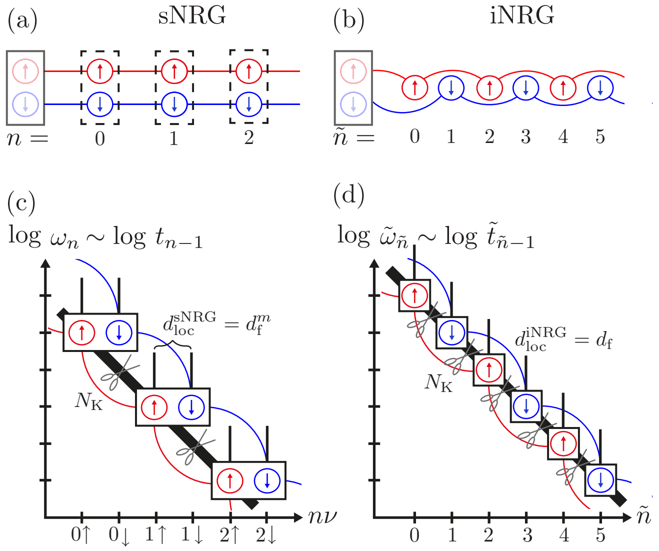

FIG. 1. Schematic illustration of standard (left) and interleaved (right) Wilson chains, for a spinful single-channel model ($m = 2$). (a) In sNRG, subsites for spin up (red) and spin down (blue) are grouped into supersites (indicated by dashed boxes), which are connected by nearest-neighbor hopping (thin lines). (b) In iNRG, subsites are interleaved in linear fashion and hopping occurs between next-nearest neighbors. n labels sNRG supersites, while $\tilde n$ labels iNRG subsites. (c) and (d) Depictions of the MPS-structure used for sNRG and iNRG: boxes represent MPS tensors, vertical thin legs represent local state spaces of dimension d_f, and thick diagonal lines represent the state spaces obtained after diagonalizing a Wilson shell and discarding all but the lowest N_K states (the truncation process is indicated by scissors). The matrix size to be diagonalized is reduced from $N_\mathrm{tot}^\mathrm{sNRG} = N_\mathrm{K}\times d_\mathrm{f}^m$ in sNRG to $N_\mathrm{tot}^\mathrm{iNRG} = N_\mathrm{K}\times d_\mathrm{f}$ in iNRG. The vertical positions of the boxes reflect, on a logarithmic scale, the characteristic energies ω_n (sNRG) and $\tilde\omega_{\tilde n}$ (iNRG) of each shell. The additional energy-scale separation within each supershell justifies the additional truncations in iNRG.

B. Interleaved Wilson chains

We now turn to the iNRG method, introduced in Ref. [23]. Its key idea is to modify the discretization scheme in such a way that energy-scale separation is achieved between all subsites associated with the same supersite, as well as between different supersites. The subsites from different subchains can then be interleaved in a linear sequence, labeled by $\tilde n \equiv (n,\nu) = m\,n + (\nu - 1) = 0,1,2,\ldots$ to form a single interleaved Wilson chain, m times longer than the corresponding standard Wilson chain [compare Figs. 1(a) and 1(b)]. The hopping matrix element $\tilde t_{\tilde n} = \tilde t_{(n,\nu)}$ describes hopping between subsites of the same flavor ν in adjacent supersites n and $n+1$. For $m > 1$, there is thus no "nearest-neighbor" hopping on the Wilson chain as in sNRG. Importantly, $\tilde t_{\tilde n}$ progressively decreases as $\tilde n$ increases. To ensure a net rate of decrease equivalent to that of a standard Wilson chain going from one supersite to the next [see Eq. (11)], we have $\tilde t_{\tilde n+m}/\tilde t_{\tilde n} \propto \Lambda^{-1/2}$. Moreover, to achieve *uniform* energy-scale separation along the interleaved chain, this decrease should occur uniformly from one subsite to the next [see Fig. 1(d)], with $\tilde t_{\tilde n+1}/\tilde t_{\tilde n} \propto \Lambda^{-1/(2m)}$. By contrast, sNRG amounts to keeping $\tilde t_{\tilde n}$ constant for all m subsites associated with the same supersite [see Fig. 1(c)]. The above behavior of $\tilde t_{\tilde n}$ can be achieved by choosing the twist parameter z_ν differently for each conduction electron flavor ν, namely $z_{\nu+1} = z_\nu - 1/(2m)$. This leads to

$$\frac{\tilde t_{\tilde n+1}}{\tilde t_{\tilde n}} = \frac{\tilde t_{n,\nu+1}}{\tilde t_{n\nu}} \overset{\text{iNRG}}{\sim} \Lambda^{-1/(2m)} \equiv \tilde\Lambda^{-1/2}, \tag{13}$$

with $\tilde t_{n,m+1} = \tilde t_{n+1,1}$. Evidently, the effective discretization parameter for iNRG is smaller than for sNRG, namely $\tilde\Lambda \equiv \Lambda^{1/m}$, thus generating scale separation from subsite to subsite within a supersite. We choose $z_m = z$, such that $\tilde t_{(n,m)} = t_n$, i.e., the iNRG hopping matrix element of the last ($\nu = m$) subsite of supersite n is identical to the sNRG hopping matrix element for that supersite. Correspondingly, the characteristic energy scale for subsite $\tilde n$ of the interleaved Wilson chain is now

$$\tilde\omega_{\tilde n} = \tilde a\tilde\Lambda^{-\tilde n/2} = a\tilde\Lambda^{-(m(n-1)+\nu)/2}\,, \tag{14}$$

where the requirement $\tilde\omega_{(n,m)} = \omega_n$ (which follows from $\tilde t_{(n,m)} = t_n$) fixes the prefactor as $\tilde a = a\tilde\Lambda^{(m-1)/2}$.

Scale separation *within* a given Wilson shell n is exploited in iNRG by performing a truncation after the addition of each new subsite (rather than only after an entire supersite of m subsites has been added, as in sNRG). With a local state space of $d_\mathrm{loc}^\mathrm{iNRG} = d_\mathrm{f}$, at each step N_K states are kept (forming a

Wilson subshell), and $N_\mathrm{K}\times(d_\mathrm{f}-1)$ ($=N_\mathrm{K}$ for $d_\mathrm{f}=2$) states are discarded.

If the eigenenergies $\tilde{E}_{\tilde{n}}$ of iNRG subshell $\tilde{n}$ are measured in rescaled units of $\tilde{\omega}_{\tilde{n}}$, the spacing of the lowest-lying levels is again of order 1. In absolute units, however, the level spacing in iNRG scales as the mth root compared with sNRG, because the m subsites are added asymmetrically (one by one with different hopping matrix elements) in iNRG, implying m times more iteration steps that lift level degeneracies. iNRG therefore constitutes a more fine-grained RG scheme, as illustrated in Fig. 7 (compare the faint red and blue lines).

C. Truncation energy

In practice, the value of N_K needed to reach a specified degree of accuracy depends sensitively on the specific physical model Hamiltonian, discretization scheme, and energy regime. This type of dependence of the accuracy on various details can be circumvented by using an *energy-based* truncation strategy [27], which we also adopt in this paper: for a given NRG calculation, we specify a fixed, dimensionless truncation energy, to be called $E^\mathrm{sNRG}_\mathrm{trunc}$ or $E^\mathrm{iNRG}_\mathrm{trunc}$, and keep only those states whose absolute (not rescaled) energies lie below $\mathrm{E}^\mathrm{sNRG}_\text{abs-trunc}=E^\mathrm{sNRG}_\mathrm{trunc}\times\omega_n$ at iteration n of an sNRG calculation, or below $\mathrm{E}^\mathrm{iNRG}_\text{abs-trunc}=E^\mathrm{iNRG}_\mathrm{trunc}\times\tilde{\omega}_{\tilde{n}}$ at iteration $\tilde{n}$ of an iNRG calculation. Using this energy-based truncation scheme, N_K becomes a *dynamical* parameter that changes from iteration to iteration in a given NRG run, in a way that depends on E_trunc, Λ, and details of the particular model under consideration (Fig. 3 below shows an example of the resulting N_K values as a function of iteration number n).

When, in our numerical analysis below, we cite sNRG values for the number of states N_K and N_tot (or for the corresponding number of symmetry multiplets, N^*_K and N^*_tot), these will refer to the geometric average over adjacent even and odd sNRG supershells chosen around a specified energy E_ref deep in the low-energy regime, where $E_\mathrm{ref}\ll T_K$. Similarly, the corresponding iNRG values refer to a geometric average over all iNRG subshells associated with both even and odd supershells near E_ref.

In general, sNRG calculations performed for the same choice of $E^\mathrm{sNRG}_\mathrm{trunc}$ yield results of comparable accuracy and degree of convergence, which are to a large extent independent of the specific model and discretization settings being considered. We have confirmed this expectation for the models studied in this paper, as discussed in detail in Sec. IV below. For sNRG, the truncation energy is therefore the key quantity controlling accuracy and convergence.

In fact, we find that this is true also for iNRG. Moreover, we find that sNRG and iNRG calculations yield results with comparable accuracy and convergence properties, provided that their truncation energies are related in such a manner that the resulting $N^\mathrm{iNRG}_\mathrm{K}$ and $N^\mathrm{sNRG}_\mathrm{K}$ values are equal "on average," i.e., after geometrically averaging over all subsites in a neighboring pair of even and odd supersites. We find empirically that this is achieved by choosing

$$E^\mathrm{iNRG}_\mathrm{trunc}=E^\mathrm{sNRG}_\mathrm{trunc}\,\Lambda^{\frac{m-1}{4m}}\,, \tag{15}$$

which implies that the parameter $E^\mathrm{iNRG}_\mathrm{trunc}$ is larger than the parameter $E^\mathrm{sNRG}_\mathrm{trunc}$. Nevertheless, the phrase "equivalent settings" includes this choice. By contrast, the simpler choice $E^\mathrm{iNRG}_\mathrm{trunc}=E^\mathrm{sNRG}_\mathrm{trunc}$ leads to a smaller average $N^\mathrm{iNRG}_\mathrm{K}$ than $N^\mathrm{sNRG}_\mathrm{K}$.

In Appendix A, we present a heuristic justification for Eq. (15). In Sec. IV, sNRG and iNRG results demonstrate explicitly that the choice of Eq. (15) leads to the desired equivalence of the number of kept states, accuracy, and convergence. In the rest of this paper, we will specify truncation energies in relation to the usual sNRG value $E_\mathrm{trunc}\equiv E^\mathrm{sNRG}_\mathrm{trunc}$, taking it to be understood that the corresponding $E^\mathrm{iNRG}_\mathrm{trunc}$ is given by Eq. (15).

D. Discarded weight

The convergence of sNRG and iNRG calculations, with a given truncation threshold E_trunc and discretization parameter Λ, can be analyzed for each model in terms of the estimated discarded weight [27] $\delta\rho_\mathrm{disc}$. As with the density matrix renormalization group (DMRG), the decay of the eigenspectrum of site-specific reduced density matrices, built from the ground state space of later iterations, can be used as a quantitative (*a posteriori*) measure of the convergence as proposed in Ref. [27]. However, in contrast to Ref. [27], where only the SIAM with $\Lambda=2$ was investigated, we wish to compare NRG calculations performed using a range of different (effective) discretization parameters Λ (or $\tilde{\Lambda}$) in different models. Since the truncation in NRG is decided on the basis of an *energy* threshold, in this context it is more natural to quantify the contributions of high-lying *energy eigenstates* to reduced density matrices, rather than analyzing the eigenspectrum of the reduced density matrices as in Ref. [27]. The details of our modified approach are presented in Appendix B.

By examining the decay of the discarded weight $\delta\rho_\mathrm{disc}$ with increasing E_trunc, and observing the corresponding convergence of physical quantities, we have found that calculations can be considered converged when $\delta\rho_\mathrm{disc}<10^{-6}$. An important advantage of defining the discarded weight in terms of the energy eigenbasis is that $\delta\rho_\mathrm{disc}$, evaluated at fixed E_trunc, is rather insensitive to changing the discretization parameter Λ.

The discarded weight analysis is particularly important in benchmarking the iNRG, because the interleaving approach appears to weaken the energy scale separation ($\tilde{\Lambda}<\Lambda$). One might then expect [23] that a larger bare Λ would be required in iNRG compared with sNRG to achieve convergence with the same discarded weight. However, our detailed study of discarded weights in Sec. IV in fact reveals the *same* degree of convergence for iNRG and sNRG when the same Λ and E_trunc are used.

E. Numerical implementation

Both sNRG and iNRG can be formulated within the framework of matrix product states (MPS), which allows for a systematic and efficient numerical implementation. Here we employ the unified tensor representation of the QSpace approach introduced in Ref. [26], in which Abelian and non-Abelian symmetries can be implemented on a generic level. The state space is labeled in terms of the symmetry eigenbasis, and the Wigner-Eckart theorem is used to determine the matrix representation of irreducible operator sets. Based on this, every (rank-3) tensor object relevant to NRG calculations splits into a tensor product of two objects that have identical data structures within the QSpace approach, operating respectively on the reduced multiplet space and the Clebsch-Gordan coefficient space. Matrix diagonalization, for example, is then only performed in the reduced multiplet space, resulting in an enormous gain of numerical efficiency.

All correlation functions presented in Sec. IV are calculated with the full-density-matrix (fdm-)NRG approach of Ref. [31]. It is established on a complete basis set [32], constructed from the discarded states of all NRG iterations. Since iNRG also produces a matrix-product-state similar to sNRG, from the point of view of fdm-NRG, iNRG cannot be distinguished from sNRG. Therefore the intrinsic multishell approach of fdm-NRG to finite temperature has the major advantage here that the subshell structure of iNRG poses no complications and is automatically taken care of. Spectral functions for the discretized model then are given from the Lehmann representation as a sum of poles, and can be calculated accurately at zero or arbitrary finite temperature. Continuous spectra are obtained by broadening the discrete data with a standard log-Gaussian kernel of frequency-dependent width [5,31].

III. MODELS

In this paper, we study three representative models with $N_c = 1,\ 2,$ and 3 spinful conduction electron channels. In Sec. IV, iNRG and sNRG are used to solve these models; the accuracy and efficiency of the two methods are then compared. Here we study models with rather high symmetries; sNRG calculations can exploit either the full symmetries of the model, or lower symmetries if desired for comparison with iNRG. We therefore assume symmetry between the bands in the following, with half-bandwidth $D_\nu \equiv D = 1$ independent of ν. This also sets the half-bandwidth as the unit of energy.

A. Single-impurity Anderson model ($N_c = 1$)

The single impurity Anderson model [1] (SIAM) describes a single correlated quantum level,

$$\hat{H}^{\rm SIAM}_{\rm imp} = \sum_\nu \varepsilon_{d\nu} \hat{d}^\dagger_\nu \hat{d}_\nu + U \hat{d}^\dagger_\uparrow \hat{d}_\uparrow \hat{d}^\dagger_\downarrow \hat{d}_\downarrow, \tag{16}$$

tunnel-coupled to a single spinful channel of conduction electrons $\hat{H}_{\rm bath}$ [Eq. (5) with $m = 2$] via

$$\hat{H}_{\rm cpl}(\{\hat{f}_{0\nu}\}) = \textstyle\sum_{k\nu} (V_{k\nu} \hat{d}^\dagger_\nu \hat{c}_{k\nu} + \text{H.c.}) \tag{17}$$

$$\equiv \sqrt{\tfrac{2D\Gamma}{\pi}}\, \textstyle\sum_\nu (\hat{d}^\dagger_\nu \hat{f}_{0\nu} + \text{H.c.}), \tag{18}$$

where $\nu \equiv \sigma \in \{\uparrow, \downarrow\} = \{+,-\}$. Here, $\hat{d}^\dagger_\nu$ creates an electron of flavor ν on the impurity, with energy $\varepsilon_{d\sigma} = \varepsilon_d + \sigma h/2$ in a Zeeman field h. For constant, flavor-independent couplings, $V_{k\nu}$, the hybridization strength is given by $\Gamma_\nu(\varepsilon) = \pi |V_\nu|^2 \rho_\nu(\varepsilon) \equiv \Gamma \Theta(D - |\varepsilon|)$ within a band of half-width $D \equiv 1$.

The SIAM possesses an SU(2) spin symmetry for $h = 0$, to be denoted by $\mathrm{SU(2)_{spin}}$, which reduces to $\mathrm{U(1)_{spin}}$ for $h \neq 0$. Moreover, at particle-hole symmetry, $\varepsilon_d = -U/2$, the SIAM possesses an SU(2) symmetry involving transformations between particles and holes, to be called $\mathrm{SU(2)_{charge}}$. This reduces to $\mathrm{U(1)_{charge}}$ for $\varepsilon_d \neq -U/2$. Depending on the symmetries allowed by the choice of model parameters, sNRG can exploit any combination of these spin and charge symmetries. In this paper, we set $h = 0$ and $\varepsilon_d = -U/2$, and employ either $\mathrm{U(1)_{spin}} \times \mathrm{U(1)_{charge}}$ or $\mathrm{SU(2)_{spin}} \times \mathrm{SU(2)_{charge}}$ symmetries.

Within iNRG, we can interleave Wilson chains for the $\nu = \uparrow$ and $\downarrow$ conduction electrons species, discretizing these separately for a given Λ using two different z shifts, $z_\uparrow = z + \frac{1}{4}$ and $z_\downarrow = z$. Since this "spin-interleaved" scheme (spin-iNRG) artificially breaks the bare symmetry between spin up and down, it reduces the $\mathrm{SU(2)_{spin}}$ symmetry to $\mathrm{U(1)_{spin}}$. Furthermore, $\mathrm{SU(2)_{charge}}$ is reduced to $\mathrm{U(1)_{charge}}$ in spin-iNRG, as the irreducible operator set for $\mathrm{SU(2)_{charge}}$ mixes spin components, and therefore cannot be defined within the state space of a single fixed-spin subsite. Consequently, spin-iNRG studies of the SIAM can employ $\mathrm{U(1)_{spin}} \times \mathrm{U(1)_{charge}}$ symmetries only.

B. Two-channel Kondo model ($N_c = 2$)

The two-channel Kondo model (2CKM) [33] features a single spin-$\frac{1}{2}$ impurity with spin $\hat{\mathbf{S}}_{\frac{1}{2}}$ coupled by antiferromagnetic Heisenberg exchange to two spinful conduction electron channels [Eq. (5) with $m = 4$]

$$\hat{H}^{\rm 2CKM}_0 = \sum_\alpha J_\alpha \hat{\mathbf{S}}_{\frac{1}{2}} \cdot \hat{\mathbf{s}}_\alpha + h S^z_{\frac{1}{2}}, \tag{19}$$

where $\hat{\mathbf{s}}_\alpha = \sum_{\sigma\sigma'} \hat{f}^\dagger_{0\alpha\sigma} \frac{\vec{\sigma}_{\sigma\sigma'}}{2} \hat{f}_{0\alpha\sigma'}$ is the conduction electron spin density at the impurity in channel $\alpha = 1,2$ (and $\vec{\sigma}$ is a vector of Pauli matrices).

In the spin sector, the 2CKM possesses an $\mathrm{SU(2)_{spin}}$ symmetry for $h = 0$, and an $\mathrm{U(1)_{spin}}$ symmetry for $h \neq 0$. In the case of particle-hole and channel symmetry ($J_1 = J_2$), the $m = 4$ flavors possess the enlarged symplectic symmetry $\mathrm{Sp(4)_{charge,channel}}$. This reduces to $[\mathrm{SU(2)_{charge}}]^2$ if channel symmetry is broken ($J_1 \neq J_2$), and further to $[\mathrm{U(1)_{charge}}]^2$ if particle-hole symmetry is broken (not considered here). Depending on the symmetries allowed by the choice of model parameters, sNRG can exploit any combination of these spin and charge symmetries. We will here set $h = 0$ and employ either the $\mathrm{U(1)_{spin}} \times [\mathrm{U(1)_{charge}}]^2, \mathrm{SU(2)_{spin}} \times [\mathrm{SU(2)_{charge}}]^2$, or $\mathrm{SU(2)_{spin}} \times \mathrm{Sp(4)_{charge,channel}}$ symmetries.

Within iNRG, the four electron flavors can be interleaved in several different ways. For example, using spin-iNRG (as described above, with $z_{\alpha,\uparrow} = z + \frac{1}{4}$ and $z_{\alpha,\downarrow} = z$), the spin symmetry is reduced to $\mathrm{U(1)_{spin}}$. Although $z_{1,\sigma} = z_{2,\sigma}$, this can only be combined with $\mathrm{U(1)_{charge}}$ symmetries in the particle sector.

Alternatively, one can interleave the spinful $\alpha = 1,2$ channels, discretizing them separately using $z_{\alpha=1,\sigma} = z + \frac{1}{4}$ and $z_{\alpha=2,\sigma} = z$ (but $z_{\alpha,\uparrow} = z_{\alpha,\downarrow}$). This "channel-interleaved" scheme (channel-iNRG) breaks the symmetry between channel 1 and 2 (even if $J_1 = J_2$) and hence the full $\mathrm{Sp(4)_{charge,channel}}$ symmetry is broken. However, $[\mathrm{SU(2)_{charge}}]^2$ symmetry can still be exploited, in combination with either $\mathrm{SU(2)_{spin}}$ or $\mathrm{U(1)_{spin}}$.

In the most asymmetric case, all four electron flavors of the 2CKM are interleaved, using $z_{1\uparrow} = z + \frac{3}{8}, z_{1,\downarrow} = z +$

$\frac{2}{8}, z_{2,\uparrow} = z + \frac{1}{8}, z_{2,\downarrow} = z$. The maximum symmetry consistent with this "flavor-interleaved" scheme (flavor-iNRG) is $\mathrm{U}(1)_{\mathrm{spin}} \times [\mathrm{U}(1)_{\mathrm{charge}}]^2$. In this paper, our iNRG studies of the 2CKM will employ the latter flavor-iNRG scheme, and also channel-iNRG with $\mathrm{SU}(2)_{\mathrm{spin}} \times [\mathrm{SU}(2)_{\mathrm{charge}}]^2$ symmetry.

The point $J_1\rho_1(0) = J_2\rho_2(0)$ is a critical point of the 2CKM, characterized by a frustration of screening that gives rise to fragile non-Fermi liquid physics [33,34]. Any finite channel anisotropy $J_1\rho_1(0) \neq J_2\rho_2(0)$ produces a crossover [34,35] to a Fermi liquid ground state, corresponding to Kondo strong coupling between the impurity and channel $\alpha = 1$ (or 2) for $(J_1\rho_1(0))/(J_2\rho_2(0)) > 1$ (or < 1). Because the interleaving in iNRG spoils the channel symmetry $[\rho_1^{\mathrm{disc}}(0) \neq \rho_2^{\mathrm{disc}}(0)]$ even in the isotropic case $J_1 = J_2$, the critical point of the 2CKM is spuriously destabilized. Fine-tuning of the ratio $J_1/J_2 \approx 1$ must then be carried out to access the critical physics [23]. This is discussed further in Sec. IV E.

C. Anderson-Hund model ($N_c = 3$)

Finally, we consider the particle-hole symmetric three-channel Anderson-Hund model (3CAHM) of Refs. [7,26,36]. The isolated 'impurity', comprising $\alpha = 1,2,3$ orbitals, each with spin $\sigma = \uparrow, \downarrow$, is described by

$$\hat{H}_{\mathrm{imp}}^{\mathrm{3CAHM}} = -J_H \hat{\mathbf{S}}^2, \tag{20}$$

where $\hat{\mathbf{S}} = \sum_\alpha \sum_{\sigma,\sigma'} d^\dagger_{\alpha\sigma} \frac{\vec{\sigma}_{\sigma\sigma'}}{2} d_{\alpha\sigma'}$ is the *total* impurity spin. Electrons of different impurity orbitals interact through the Hund coupling, J_H, in Eq. (20).

Each impurity orbital with flavor $\nu = (\alpha,\sigma)$ is tunnel-coupled to a conduction electron band of the same flavor, via Eq. (18); overall there are $m = 6$ electronic flavors. The large local state space $d_{\mathrm{loc}}^{\mathrm{sNRG}} = 64$ for the 3CAHM means that iterative diagonalization in *state* space (rather than multiplet space) is practically intractable for sNRG. However, this 3CAHM possesses large symmetries that can be optimally exploited in sNRG: $\mathrm{SU}(2)_{\mathrm{spin}}$ symmetry in the spin sector, and $\mathrm{Sp}(6)_{\mathrm{charge,channel}}$ symmetry in the particle-hole/channel sector. The 64 states describing a single Wilson supersite reduce to a mere four multiplets in this case.

The $\mathrm{Sp}(6)_{\mathrm{charge,channel}}$ symmetry reduces to $\mathrm{U}(1)_{\mathrm{charge}} \times \mathrm{SU}(3)_{\mathrm{channel}}$ if particle-hole symmetry is broken, or to $[\mathrm{SU}(2)_{\mathrm{charge}}]^3$ if channel symmetry is broken. Exploiting one of these three large symmetries is essential when using sNRG. For iNRG, one again has several options for interleaving. We will consider channel-iNRG with $\mathrm{SU}(2)_{\mathrm{spin}} \times [\mathrm{SU}(2)_{\mathrm{charge}}]^3$ symmetry, and full flavor-iNRG with $\mathrm{U}(1)_{\mathrm{spin}} \times [\mathrm{U}(1)_{\mathrm{charge}}]^3$ symmetry. A major advantage of iNRG is that such models can be solved even when no large symmetries are available [cf. yellow dashed curve in Fig. 5(b) that shows the spectral function of the 3CAHM calculated with iNRG and $\mathrm{U}(1)_{\mathrm{spin}} \times [\mathrm{U}(1)_{\mathrm{charge}}]^3$ symmetry].

IV. RESULTS

In the following, we present a comprehensive comparison of iNRG and sNRG for the three models introduced in Sec. III. We begin in Sec. IV A by summarizing our main conclusions, referring only briefly to the relevant figures. We then offer a detailed analysis of the figures to substantiate our main results in the subsequent sections. In particular, we compare iNRG and sNRG by examining the number of kept multiplets in Sec. IV B, the efficiency of the calculations in Sec. IV C, and the accuracy/convergence of the results in Sec. IV D. The take-home message is that iNRG offers significant improvements in efficiency without compromising accuracy and convergence properties.

A. Overview

We perform calculations in which, for a given model, discretization parameter Λ, and choice of exploited symmetries, the truncation energies of iNRG and sNRG are related by Eq. (15) . This use of *equivalent settings* allows for optimal comparability, because it ensures that, on average, the same number of states are kept at each iteration in both methods. The number of kept *multiplets*, N_{K}^*, is therefore also the same on average—as demonstrated explicitly in Figs. 2(a)–2(c) and 3.

Number of multiplets. N_{K}^*, and thus also N_{K}, is found to increase roughly exponentially with E_{trunc} and also with the number of conduction electron channels N_c [Figs. 2(a)–2(c) and 4]. This scaling is common to both iNRG and sNRG. It simply reflects the fact that the number of many-body eigenstates of a gapless system grows exponentially with energy, with an exponent that increases linearly with N_c. Since we exploit symmetries and conserved quantities in the calculations, the number of kept *multiplets* N_{K}^* is far smaller than the number of kept *states* N_{K} in both iNRG and sNRG. When iNRG and sNRG use the same symmetry setting, the total number of multiplets to be diagonalized at each iteration, N_{tot}^*, is far smaller for iNRG than sNRG [Figs. 2(d)–2(f)], due to the intermediate truncations in iNRG. However, iNRG cannot always exploit the full model symmetries due to the interleaving process. As a consequence there can be an efficiency tradeoff in iNRG: the advantage of a reduced local state space comes at the cost of fewer symmetries being available to exploit. This is shown by Figs. 2(d)–2(f), where N_{tot}^* for the most efficient iNRG calculation is essentially the same as that of the best sNRG calculation (exploiting all symmetries) in each case [in fact, N_{tot}^* is actually lower in sNRG for the SIAM in panel (d)].

Efficiency. The total CPU time for a given iNRG calculation is smaller than that of the corresponding sNRG calculation with equivalent settings [Figs. 2(g)–2(i)]. In fact, with $\Lambda = 4$, spin-iNRG for the SIAM, spin and channel-iNRG for the 2CKM and channel-iNRG calculations for the 3CAHM are also more efficient than the *best* sNRG calculations exploiting full symmetries. Even though N_{tot}^* is typically similar or even lower for the best sNRG compared to the best iNRG calculations, the book-keeping overheads involved in exploiting symmetries can outweigh the potential gains of doing so (this is especially pronounced for smaller E_{trunc}). In general, the gain in iNRG efficiency becomes more significant as the number of flavors increases. Importantly, some low-symmetry, many-band models that are prohibitively expensive for sNRG can still be tackled with iNRG.

Accuracy and convergence. Remarkably, these gains in efficiency do not compromise accuracy and convergence properties. To establish this, we performed extensive comparisons

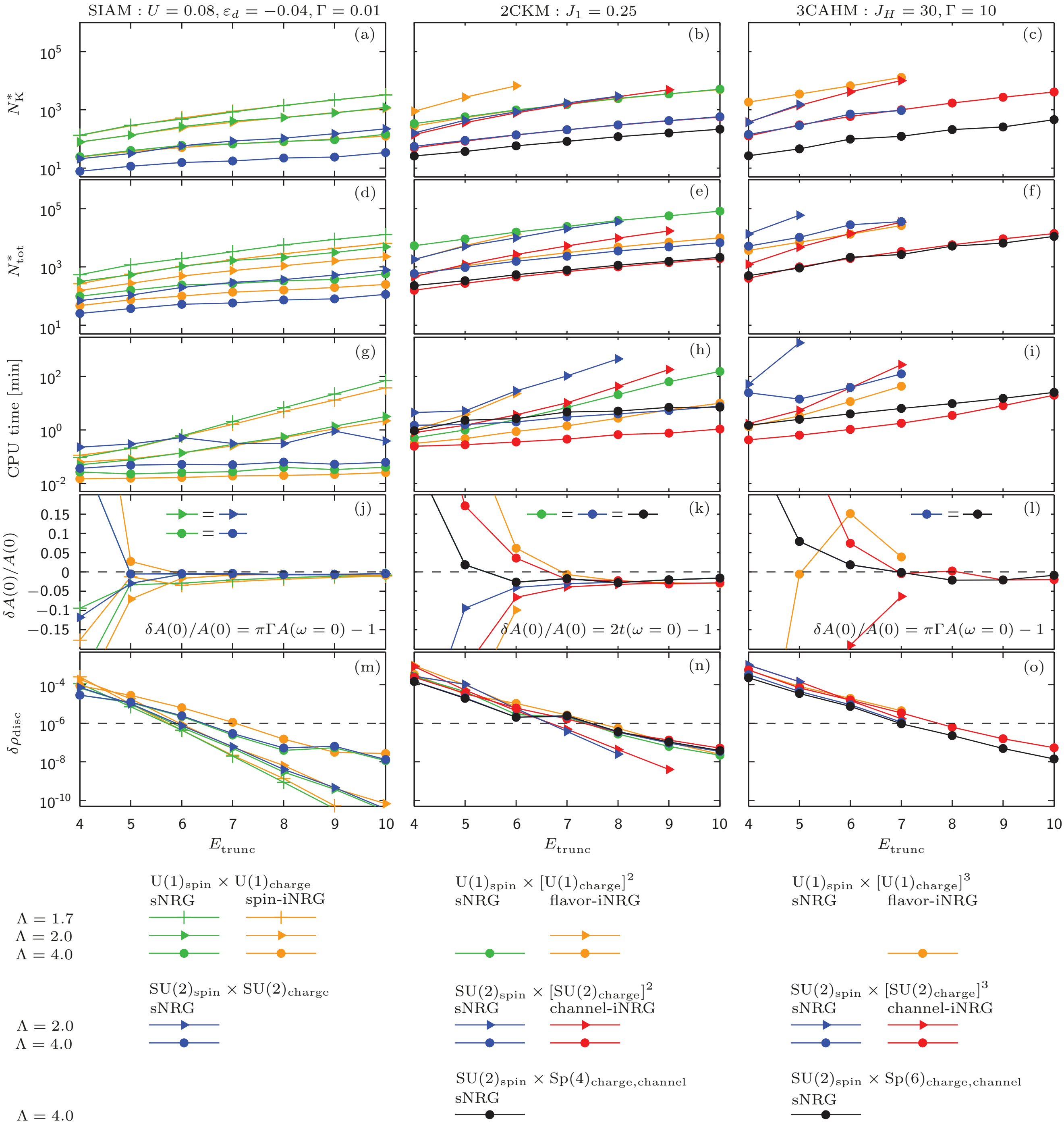

FIG. 2. Comparison of sNRG and iNRG for three models: SIAM (left column), 2CKM (middle column), and 3CAHM (right column). (a)–(c) The number of kept multiplets, N_K^*; (d)–(f) the total number of multiplets generated during an NRG step, N_{tot}^*; (g)–(i) the total CPU time for one NRG run; (j)–(l) the relative deviations $\delta A(0)/A(0)$ of correlation functions at the Fermi energy $\omega = 0$ from their exact values [cf. Eqs. (21)]; and (m)–(o) the discarded weight $\delta\rho_{disc}$ (the horizontal dashed lines indicate the convergence threshold). All quantities (computable with a maximum memory of 128 GB) are plotted versus E_{trunc} ($\equiv E_{trunc}^{sNRG}$), for $\Lambda = 1.7$ (crosses), 2.0 (triangles), and 4.0 (circles). Each symmetry setting is identified by a particular color in iNRG and sNRG. iNRG results have been geometrically averaged over all interleaved flavors. Data for N_K^* and N_{tot}^* have been geometrically averaged over even and odd Wilson shells at an energy scale $E_{ref} = 5 \times 10^{-8} D \ll T_K$. We used $z = 0$ in all cases except for (j)–(l), where data for $z = 0$ and 0.5 have been averaged. An exception is the flavor-iNRG data point at $E_{trunc} = 7$ in (l), which was obtained for $z = 0$ without z averaging ($z = 0.5$ exceeded memory resources). In (j)–(l), sNRG results with the same Λ but different symmetry settings coincide.

between iNRG and sNRG using equivalent settings [see Figs. 2(j)–2(l), 2(m)–2(o), and 5].

The accuracy of iNRG was established directly, by monitoring the deviation of calculated physical quantities from certain exact results. In particular, we studied the value of the impurity spectral function (or t matrix) at the Fermi level, relative to known analytic results [Figs. 2(j)–2(l)]. The quality of the results improves with increasing E_{trunc} as expected, and exact results are reproduced to within a few percent for $E_{\text{trunc}} > 7$ in both sNRG and iNRG. This conclusion is further supported by comparisons of the full frequency dependence of impurity spectral functions in Fig. 5.

Furthermore, our analysis of the discarded weight shows that both iNRG and sNRG calculations are effectively converged for $E_{\text{trunc}} > 7$ [Figs. 2(m)–2(o)]. This demonstrates explicitly that the states discarded at intermediate steps in iNRG do not contribute appreciably to low-energy eigenstates at later iterations, thus validating the more fine-grained RG scheme employed by iNRG.

Artificially broken symmetries. Finally, we examined the tuning protocol employed in iNRG to restore channel symmetries that are broken artificially by the interleaved discretization (see Fig. 6). Such channel symmetries are of course not always relevant perturbations (an example is the 3CAHM, where the same basic low-energy physics arises even in the channel-anisotropic case). The worst-case scenario for iNRG emerges in the vicinity of a quantum critical point, where channel asymmetries generate a relevant RG flow to a different fixed point [33,34]. The classic exemplar is the 2CKM, whose frustrated critical point occurs precisely at $J_1\rho_1(0) = J_2\rho_2(0)$. In iNRG, where $\rho_1^{\text{disc}}(0) \neq \rho_2^{\text{disc}}(0)$, the ratio J_1/J_2 must be tuned to access this physics, but is found in practice to deviate from its exact value by only $\sim$1%. We also show that the critical point can be located exponentially rapidly in the number of iNRG runs, keeping calculation overheads to a minimum.

B. Number of kept multiplets

The key difference between sNRG and iNRG is the size of the local state space, i.e., $d_{\text{loc}}^{\text{sNRG}} = d_{\text{f}}^{m}$ versus $d_{\text{loc}}^{\text{iNRG}} = d_{\text{f}}$. However, to compare fairly the relative efficiency, we must ensure that both calculations are of comparable accuracy. By choosing the "same" truncation energies in iNRG and sNRG [via Eq. (15)], a comparable number of multiplets is kept in both calculations, as argued in Sec. II C. Here we present data to substantiate this. Moreover, the consequence of this choice is that sNRG and iNRG calculations are of equivalent accuracy, as demonstrated explicitly below in Sec. IV D.

Figures 2(a) and 2(c) show N_{K}^{*} obtained for the SIAM, 2CKM, and 3CAHM, with several different choices of Λ, and employing various symmetry settings. In all cases, we find that $N_{\text{K}}^{*,\text{iNRG}}$ and $N_{\text{K}}^{*,\text{sNRG}}$ are comparable when the same symmetry setting is used. However, note that the different iNRG subshells contribute unequally to their geometric average, because the absolute truncation energy changes from subshell to subshell in iNRG, as explained in Sec. II C. This is illustrated in Fig. 3, which shows N_{K}^{*} as function of Wilson shell index n for the 2CKM. For iNRG, the number of multiplets kept after adding the first channel (red dashed line) is smaller than the number of multiplets kept after adding the second channel (red dash-dotted), but their geometric average (red solid) is rather similar to the number of kept multiplets in the corresponding sNRG calculation (blue solid line) for all n.

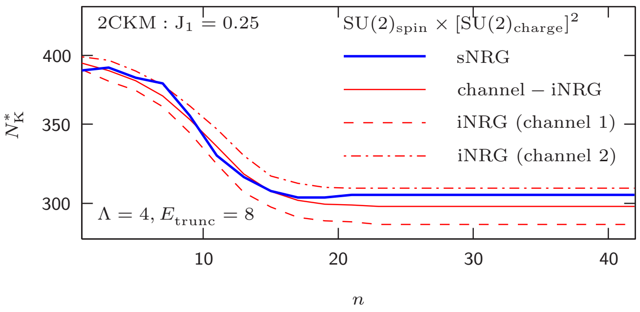

FIG. 3. Number of kept multiplets N_{K}^{*} vs Wilson shell index n for the 2CKM within the $\text{SU(2)}_{\text{spin}} \times [\text{SU(2)}_{\text{charge}}]^2$ symmetry setting. For iNRG (red), the number of multiplets kept after adding channel 1 (dashed) or channel 2 (dash-dotted) are shown separately, as well as their geometric average (solid). sNRG results are shown in blue for comparison. All results are geometrically averaged over even and odd iterations.

Furthermore, Figs. 2(a) and 2(c) confirm that the total number of kept multiplets N_{K}^{*} depends exponentially on E_{trunc}, with a growth exponent that increases with N_c [the slope of the line increases from Figs. 2(a) to 2(c)]. This behavior is expected for the many-body eigenstates of a gapless system, whose number increases exponentially with energy.

Naturally, exploiting larger symmetries means that fewer multiplets are kept for a given E_{trunc}. [For example, in Fig. 2(c) for $\Lambda = 4$, the black circles lie well below the red and blue circles.] This reduction of the multiplet space arises by splitting off large Clebsch-Gordan spaces. We also note that smaller Λ, which reduces energy-scale separation between iterations, leads to larger N_{K}^{*}, and to a faster increase of N_{K}^{*} with E_{trunc}. [For example, in Fig. 2(b), the blue and red triangles for $\Lambda = 2$ lie above the blue and red circles for $\Lambda = 4$, and rise with a greater slope.]

Furthermore, the number of kept *states*, N_{K} (which is independent of the symmetry settings used), increases roughly exponentially with the number of conduction electron channels, m. This is confirmed in Fig. 4, which shows N_{K} for the multichannel Kondo model (N_{c}-CKM) and the multichannel Anderson-Hund model (N_{c}-CAHM), with $N_{\text{c}} = 1,2,3$ spinful channels [these models are the generalizations of Eqs. (19) and (20) to the case of N_{c} channels]. Figure 4 also shows that the description of certain multichannel fixed points requires a greater number of kept states than others, reflecting their relative complexity. For example, the frustrated non-Fermi liquid fixed points of the N_{c}CKM (with $N_{\text{c}} \geqslant 2$) require a larger N_{K} than the corresponding Fermi liquid fixed points of the N_{c}CAHM at $E_{\text{trunc}} = 7$.

These results confirm that the exponential scaling of required computational resources with m in both sNRG and iNRG cannot be avoided—it simply reflects elementary state-counting properties for gapless multichannel systems. However, the efficiency of the calculation for a given model can be substantially improved by exploiting symmetries in sNRG, or by interleaving flavors in iNRG, as now discussed.

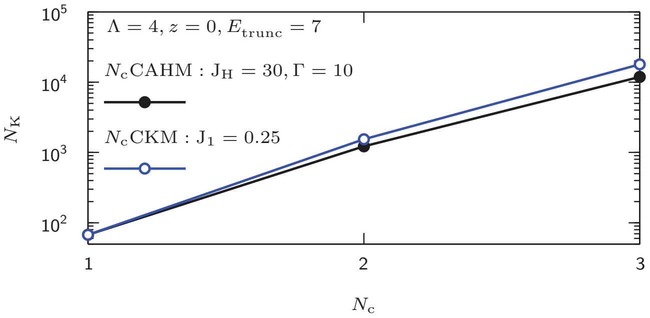

FIG. 4. Number of kept *states* $N_{\rm K}$ at the low-energy fixed point of the $N_{\rm c}$CAHM (black) and $N_{\rm c}$CKM (blue), showing a roughly exponential increase with the number of channels, $N_{\rm c}$. Results were obtained with sNRG and have been geometrically averaged over even and odd Wilson shells at energy scale $E_{\rm ref} = 5 \times 10^{-8} D \ll T_K$.

C. Efficiency

The *total* number of multiplets, $N^*_{\rm tot}$, generated in NRG near the low-energy fixed point of the three models, is plotted as a function of $E_{\rm trunc}$ in Figs. 2(d)–2(f). As with $N^*_{\rm K}$, the size of $N^*_{\rm tot}$ depends on the particular model under consideration, Λ, $E_{\rm trunc}$, and the symmetry setting used. Additionally, we now also see a dramatic difference between iNRG and sNRG. When the same symmetry setting is used, $N^{*,\rm iNRG}_{\rm tot}$ is far smaller than $N^{*,\rm sNRG}_{\rm tot}$, because $d^{\rm iNRG}_{\rm loc}$ is smaller than $d^{\rm sNRG}_{\rm loc}$. [For example, the red data points lie clearly below the blue data points in Fig. 2(f) for the 3CAHM and in Fig. 2(e) for the 2CKM.] Moreover, then also the ratio $N^{*,\rm sNRG}_{\rm tot}/N^{*,\rm iNRG}_{\rm tot}$ grows exponentially with the number of interleaved flavors. For a given model and symmetry, $N^{*,\rm sNRG}_{\rm tot}/N^{*,\rm iNRG}_{\rm tot}$ would therefore be larger for full flavor-iNRG than channel-iNRG. However, note that in general $N^*_{\rm tot}$ itself might be smallest for channel-iNRG, meaning that the optimal strategy might involve keeping some symmetries at the expense of interleaving fewer flavors. An example of this is seen clearly for the 2CKM in Figs. 2(e) and 2(f), where red dots lie below orange dots.

These trends in $N^*_{\rm tot}$ are reflected in the CPU time plotted in Figs. 2(g)–2(i), which is the ultimate measure of calculation efficiency. The total CPU time for an NRG calculation is generally dominated by matrix diagonalizations (especially for large $E_{\rm trunc}$), and therefore scales as $\sim(N_{\rm tot})^3$. Since $N^*_{\rm K}$ and $N^*_{\rm tot}$ grow with $E_{\rm trunc}$, so too does the CPU time – the faster so with smaller Λ. For small $E_{\rm trunc}$, however, numerical overheads can also have a noticeable influence. [For example, in Fig. 2(e) for $N^*_{\rm tot}$, the green and orange circle points for $\Lambda = 4$ show a separation that is quite large and approximately constant; by contrast, Fig. 2(h) shows an increasing difference in the CPU time with increasing $E_{\rm trunc}$. At large $E_{\rm trunc}$, the difference is essentially attributable to the difference in $N^*_{\rm tot}$ alone. At small $E_{\rm trunc}$, the numerical overhead in iNRG can presumably be attributed to larger Wilson chain lengths.]

The maximum efficiency gain of iNRG over sNRG in terms of CPU time occurs if no symmetries are used in either iNRG or sNRG. This gain is then of order $\sim d_{\rm f}^{3(m-1)}/m$, where the factor of $1/m$ arises because the interleaved Wilson chain is m times longer than the standard Wilson chain. Similarly, the corresponding gain in terms of memory resources is given by $\sim d_{\rm f}^{2(m-1)}$, here without the factor of $1/m$, since memory is required on the level of a specific NRG iteration rather than for the whole calculation. The following table summarizes the theoretical maximum gain relative to sNRG (in the absence of symmetries) obtained with channel-iNRG and flavor-iNRG for models with $N_{\rm c} = 1,2,3$:

No. spinful channels	No. channels interleaved	Max. speedup factor (CPU)	Max. gain in memory
$N_{\rm c} = 1$	$N_{\nu=\sigma} = 2$	4	4
$N_{\rm c} = 2$	$N_{\nu=\alpha} = 2$	32	16
	$N_{\nu=\alpha\sigma} = 4$	128	64
$N_{\rm c} = 3$	$N_{\nu=\alpha} = 3$	1365	256
	$N_{\nu=\alpha\sigma} = 6$	5461	1024

When symmetries are exploited in the calculations, the efficiency gain for iNRG over sNRG is reduced, relative to the value cited in the above table, because the local Hilbert space of each supersite in sNRG (or subsite in iNRG) is organized into *multiplets* instead of states. The factor $d_{\rm f}^{3(m-1)}/m$, which was based on a *state*-counting argument, is then effectively reduced. Note, however, that handling and bookkeeping of Clebsch-Gordan coefficient spaces also introduces a numerical overhead. For very small $E_{\rm trunc}$, this can even outweigh the efficiency gains of exploiting symmetries. However, the symmetry gains grow with increasing $E_{\rm trunc}$ (which leads to increasingly large block sizes for reduced matrix elements), and eventually always dominate compared to book-keeping overheads. [For example, in Fig. 2(h) for $\Lambda = 4$, the green circles lie below the blue circles for small $E_{\rm trunc}$, but cross at $E_{\rm trunc} \simeq 6$. For large $E_{\rm trunc}$, the most efficient sNRG calculations are those that exploit the largest symmetries (the black circles start crossing the blue circles at $E_{\rm trunc} = 10$).]

Ultimately, when the same symmetries are used for both calculations, iNRG clearly requires far smaller CPU time than sNRG for a given Λ and $E_{\rm trunc}$, see Figs. 2(h) and 2(i). This effect becomes more pronounced with increasing $E_{\rm trunc}$.

The models considered here have high intrinsic symmetries, which can be more fully exploited in sNRG than iNRG. The "best case" scenario for sNRG, in which the *full* model symmetries are exploited, are shown as the blue data points in the first column of Fig. 2 and as black points in the second and third columns of Fig. 2. For $N_{\rm c} = 1$ [panel (d)], this optimal sNRG generates a slightly smaller $N^*_{\rm tot}$ than the best corresponding iNRG calculation (for a given Λ and $E_{\rm trunc}$). However, when the number of channels is increased to $N_{\rm c} = 2$ or 3 [panels (e) and (f)], we find similar $N^*_{\rm tot}$ for the best iNRG calculations (red dots) and the best sNRG calculations (black dots). Nevertheless, for the range of $E_{\rm trunc}$ values used here, the total CPU times [panels (h) and (i)] for $\Lambda = 4$ calculations employing channel-iNRG (red dots) are still lower than for sNRG (black dots), even when full symmetries are exploited in sNRG (the difference is attributable to additional bookkeeping costs incurred when handling large symmetries in sNRG).

The benefits of exploiting symmetries increase for larger $N^*_{\rm tot}$ and hence $E_{\rm trunc}$. As a consequence, we find that the CPU time increases with $E_{\rm trunc}$ slower for full-symmetry sNRG than for iNRG. For example, for $N_{\rm c} = 3$ and $\Lambda = 4$, in panel (f) for $N^*_{\rm tot}$ the black (sNRG) and red (iNRG) dots are approximately equivalent, while in panel (i) for the CPU times, the black dots lie well above the red dots for small $E_{\rm trunc}$, but then rise more slowly with $E_{\rm trunc}$, so that both roughly coincide for $E_{\rm trunc} = 10$. Similarly, for $N_{\rm c} = 1$ and $\Lambda = 2$, in panel (g) for $N^*_{\rm tot}$ the blue triangles (sNRG) start above the orange triangles (iNRG) for small $E_{\rm trunc}$, but rise more slowly and end up below the latter for $E_{\rm trunc} \gtrsim 7$, showing that full-symmetry sNRG can sometimes be the most efficient method. We also anticipate that full-symmetry sNRG for $N_{\rm c} = 3$ [panel (i)] would be more efficient than iNRG for $E_{\rm trunc} \gtrsim 10$.

Finally, we note that the optimal iNRG calculation does not necessarily involve interleaving all possible flavors, due to the tradeoff in lowered symmetries. Indeed, making partial use of interleaving and partial use of symmetries can yield the best results, as seen, for example in panels (h) and (i) for the CPU times of $N_{\rm c} = 2$ and 3, respectively, where the red symbols (channel-iNRG) lie below the corresponding orange symbols (flavor-iNRG).

D. Accuracy

As highlighted above, the iNRG scheme is more efficient due to the intermediate truncations along the interleaved Wilson chain, which results in the smaller local state space $d_{\rm loc} = d_{\rm f}$ at each step (if all flavors are interleaved). A key question is whether these intermediate truncations adversely affect the accuracy of iNRG results. In the following, we show that, for the same model and same Λ, with truncation energies set equal as in Eq. (15), we obtain results with similar accuracy and convergence properties for both iNRG and sNRG.

The absolute accuracy of both iNRG and sNRG can be directly assessed from calculated physical quantities. In particular, we focus on $T = 0$ correlation functions. For the particle-hole symmetric SIAM and 3CAHM, the impurity spectral function $A(\omega) = -\frac{1}{\pi}{\rm Im}\langle\langle \hat{d}_\nu; \hat{d}^\dagger_\nu\rangle\rangle_\omega$ is pinned by the Friedel sum rule at the Fermi level, $\omega = 0$. The exact analytic result [1] is $\pi\Gamma A(0) = 1$. As a measure of the accuracy in NRG, we therefore consider the relative deviation at the Fermi energy,

$$\delta A(0)/A(0) = \pi\Gamma A(0) - 1, \tag{21a}$$

shown in Figs. 2(j) and 2(l). For the 2CKM, we consider the spectrum $t(\omega) = -\pi\rho(\omega){\rm Im}T(\omega)$, where $T(\omega)$ is the scattering t matrix. Again, the spectrum is pinned at the low-energy non-Fermi liquid fixed point; the exact analytic result [37] is $t(0) = \frac{1}{2}$. In Fig. 2(k), we therefore consider the relative NRG deviation at the Fermi energy,

$$\delta A(0)/A(0) = 2t(0) - 1\ . \tag{21b}$$

We find that iNRG and sNRG perform similarly, recovering exact results to within a few percent for $E_{\rm trunc} > 7$. For each case studied, iNRG appears to deviate somewhat stronger from $\delta A(0)/A(0) = 0$ for $E_{\rm trunc} < 7$ than sNRG; but approximately equivalent results are obtained for $E_{\rm trunc} > 7$. Even when interleaving all 6 flavors in the 3CAHM, using Abelian symmetries only, we similarly anticipate that $\delta A(0)/A(0)$ will converge to 0 for sufficiently large $E_{\rm trunc}$. [This is supported in Fig. 2(l) by the orange data point at $E_{\rm trunc} = 7$, which was calculated for $z = 0$ only.]

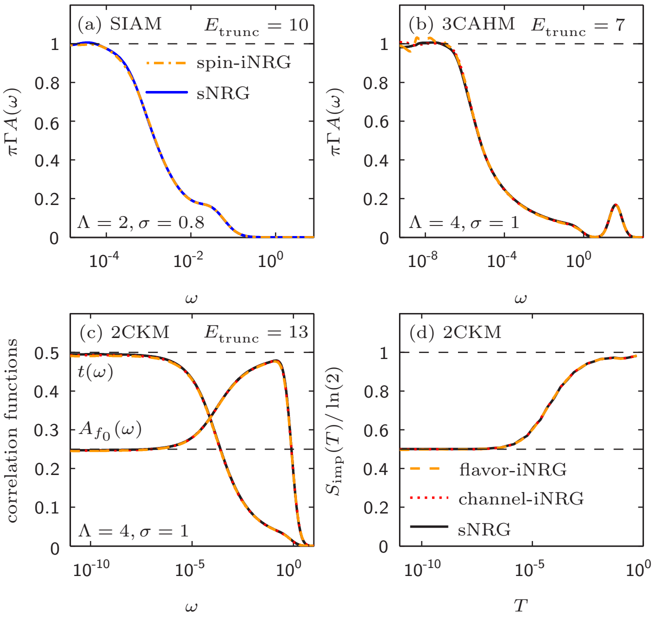

FIG. 5. Comparison of physical quantities calculated with iNRG and sNRG. (a) Impurity spectral function $\pi\Gamma A(\omega)$ at $T = 0$ for the SIAM; (b) impurity spectral function $\pi\Gamma A(\omega)$ at $T = 0$ for the 3CAHM; (c) spectrum of the t matrix $t(\omega)$ and the correlator $A_{f_0}(\omega)$ at $T = 0$ for the 2CKM; (d) impurity contribution to the entropy, $S_{\rm imp}(T)$, for the 2CKM. For the dynamical correlators shown in (a)–(c), the protocol of Ref. [31] was used to broaden discrete data, using a broadening parameter of $\sigma_{\rm broad} = 0.8$ or 1 for $\Lambda = 2.0$ or 4.0, respectively. All quantities were z-averaged over $z = 0$ and 0.5, except for the flavor-interleaved 3CAHM spectral function in (b), which was only calculated for $z = 0$ ($z = 0.5$ exceeded memory resources). The observed low-frequency oscillations are therefore an artifact of underbroadening, and would be removed by additional z averaging or use of a larger $\sigma_{\rm broad}$.

This conclusion is further substantiated by Fig. 5, which shows the full frequency dependence of dynamical correlation functions at $T = 0$ in panels (a)–(c), and the temperature dependence of the impurity entropy in panel (d). For the SIAM in panel (a), the iNRG and sNRG impurity spectral functions are essentially indistinguishable for $E_{\rm trunc} = 10$ and $\Lambda = 2$, at all frequencies. For the 3CAHM in panel (b), channel-iNRG and sNRG results for the impurity spectral function are again indistinguishable for $E_{\rm trunc} = 7$ and $\Lambda = 4$. Flavor-iNRG shows some oscillations on the lowest energy scales due to underbroadening: the iNRG calculation was performed only for $z = 0$. Obtaining a completely smooth curve would either require additional z averaging (but $z = 0.5$ exceeded memory resources) or the use of a larger broadening, $\sigma_{\rm broad}$. Panel (c) shows the spectrum of the t matrix $t(\omega)$, and the local bath spectral function $A_{f_0}(\omega) = -\frac{1}{\pi}{\rm Im}\langle\langle \hat{f}_{0\nu}; \hat{f}^\dagger_{0\nu}\rangle\rangle_\omega$ for the 2CKM. At $E_{\rm trunc} = 13$ for $\Lambda = 4$, both iNRG and sNRG yield equivalent and highly accurate results. Finally, panel (d) confirms that thermodynamic quantities (here illustrated for the impurity contribution to the total entropy) are accurately reproduced using both iNRG and sNRG for the 2CKM. In particular, the nontrivial residual entropy [37] $S_{\rm imp}(T = 0) = \frac{1}{2}\ln(2)$ is correctly reproduced.

In Figs. 2(m)–2(o), we examine the convergence of both iNRG and sNRG calculations, analyzed quantitatively in terms of the NRG discarded weight $\delta\rho_{\rm disc}$ (see Sec. II D). As expected, the discarded weight decays exponentially with increasing $E_{\rm trunc}$. The calculations are considered fully converged when $\delta\rho_{\rm disc} < 10^{-6}$, which is reached in all cases at around $E_{\rm trunc} \approx 7$. No qualitative changes occur in physical results on further increasing $E_{\rm trunc}$ [panels (j)–(l)]. Figures 2(m)–2(o) show clearly that the convergence behavior of iNRG is equivalent to that of sNRG, implying that the states additionally discarded by iNRG at intermediate steps do *not* have appreciable weight in the eigenstates of later iterations. Indeed, the discarded weights for iNRG (orange and red symbols) and sNRG (green, blue and black symbols) for the same Λ are approximately equal. [The only exception is seen in panel (m), for $N_{\rm c} = 1$ and $\Lambda = 4$, where the discarded weight differences between sNRG (green circles) and iNRG (orange circles) are apparently somewhat larger. We attribute this to inaccuracies in the estimation of the discarded weight, since, by far, the smallest number of data points (diagonal weights ρ_s) were available for the extrapolation in this case.]

For $\delta\rho_{\rm disc} \gtrsim 10^{-6}$, i.e., above the convergence threshold, the discarded weights behave similarly for *all* NRG calculations irrespective of the choice of Λ; below this threshold, the behavior becomes somewhat dependent on Λ: for a given $E_{\rm trunc}$, larger Λ yields a larger discarded weight both for iNRG and sNRG [panels (m) and (n)]. The reason for this is that the spectrum of *rescaled* eigenenergies in NRG shows a Λ dependence for higher energies: while rescaling is designed to ensure that the low-energy regime (dominated by single-particle excitations) of the rescaled eigenspectrum is almost Λ-independent, it stretches apart the high-energy regime (dominated by many-particle excitations). High-energy states are therefore shifted up more for larger Λ. The consequence is that, on increasing $E_{\rm trunc}$ and Λ, the weight of the reduced density matrices is shifted to higher rescaled energies. This means that the slope κ of the dashed red line in Fig. 8 would decrease, causing an increase in the total integrated discarded weight $\delta\rho_{\rm disc}$.

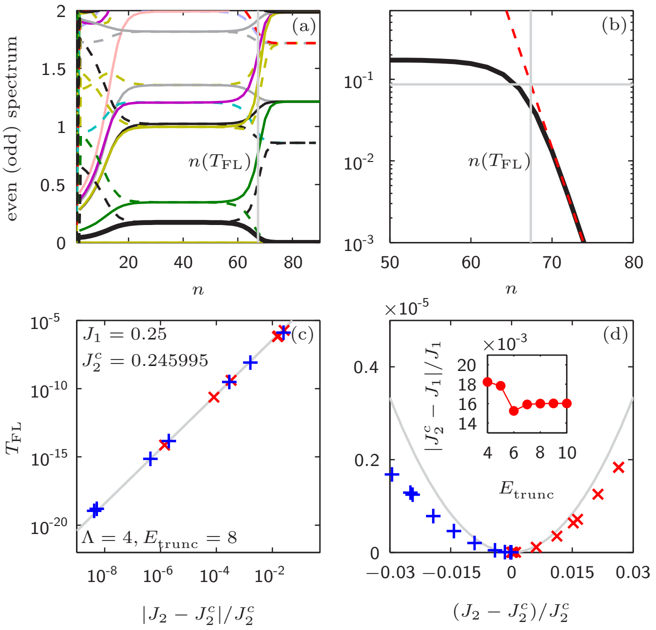

FIG. 6. Fine tuning in iNRG for the 2CKM (a) Flow of iNRG many-particle energies with Wilson shell index n [solid (dashed) lines for even (odd) n] for the 2CKM. Different colors correspond to states with different quantum numbers. (b) The Fermi liquid crossover scale $T_{\rm FL}$ can be extracted from the flow of the first excited state (thick black line): we fit its large-n behavior with a power law (dashed red line), take $n(T_{\rm FL})$ to be the iteration number [vertical grey line in (a) and (b)] at which this power law reaches half of the fixed-point value of this state (horizontal grey line), and define the Fermi liquid scale as $T_{\rm FL} = \omega_{n(T_{\rm FL})}$. In (c) and (d), the resulting values of $T_{\rm FL}$ are plotted as function of $J_2 - J_2^c$ on a log-log or linear plot, respectively, using red (blue) symbols for $J_2 > J_2^c$ ($< J_2^c$). Grey lines give the asymptotic form $T_{\rm FL} \sim (J_2 - J_2^c)^2$. By using an extrapolative protocol, the critical coupling J_2^c can be located exponentially rapidly in the number of separate iNRG runs. [Inset to (d)] The difference between the critical coupling J_2^c and J_1, plotted as a function of the truncation energy.

E. Fine tuning in iNRG

If a given model possesses an exact flavor symmetry—and furthermore, if the breaking of this flavor symmetry is an RG *relevant* perturbation—iNRG must be combined with parameter fine tuning. This is because the asymmetric discretization required to interleave different Wilson chains in iNRG artificially breaks bare flavor symmetries, albeit rather weakly. However, effective channel symmetry in the discretized model can be restored through the fine-tuning of couplings [23].

A prime example is the 2CKM, for which channel symmetry-breaking is relevant [33,34]. The critical point of the 2CKM is realized at precisely $\rho_1(0)J_1 = \rho_2(0)J_2$, embodying the frustration responsible for its non-Fermi liquid properties. In sNRG, channel symmetry is exactly preserved: $\rho_1^{\rm disc}(\varepsilon) = \rho_2^{\rm disc}(\varepsilon)$, and so the critical physics is accessible along the line $J_1 = J_2$ (only the Kondo temperature $T_{\rm K}^{\rm 2CK}$ is affected by the actual value chosen for $J_1 = J_2$). However, we note that even in sNRG, the precise value of $\rho_\alpha^{\rm disc}(0)J_\alpha$ can deviate very slightly from the bare value $\rho_\alpha(0)J_\alpha$, due to the discretization. Although the $T_{\rm K}^{\rm 2CK}$ obtained in sNRG might therefore also be slightly different from the true value, it should be emphasized that the *universal* low-energy physics is identical.

Likewise, $\rho_\alpha^{\rm disc}(0)J_\alpha$ deviates from $\rho_\alpha(0)J_\alpha$ in iNRG. However, the important difference is that $\rho_1^{\rm disc}(0)J_1 \neq \rho_2^{\rm disc}(0)J_2$, even when $\rho_1(0)J_1 = \rho_2(0)J_2$. In the presence of this small channel asymmetry perturbation, the critical point is destabilized, leading to a flow *away* from the non-Fermi liquid fixed point, and toward a stable Fermi liquid fixed point [34,35,37]. The temperature/energy scale characterizing this Fermi liquid crossover is denoted $T_{\rm FL}$. To access the critical physics for a given J_1, one must therefore fine tune the value of $J_2 \to J_2^c$ such that $T_{\rm FL} \to 0$. In principle, $T_{\rm FL}$ can be extracted from any physical quantity; it can also be extracted directly from the flow of NRG many-particle energies, as shown in Figs. 6(a) and 6(b) (see caption for details).

A very efficient extrapolative tuning protocol can be employed if the functional dependence of $T_{\rm FL}$ on $J_2 - J_2^c$ is known analytically. In the case of the 2CKM, it is known [37] that $T_{\mathrm{FL}} \sim (J_2 - J_2^c)^2$ when $T_{\mathrm{FL}} \ll T_{\mathrm{K}}^{\mathrm{2CK}}$. This can be exploited by adopting the following protocol (somewhat similar to Newton's method for finding roots from a linear fit): the lowest two values of T_{FL} extracted from previous iNRG runs are used to fit a parabola; the trial value of J_2 for the next iNRG run is then given by the minimum of the parabola. This protocol is illustrated in Figs. 6(c) and 6(d). J_2 converges to the critical value J_2^c exponentially rapidly in the number of separate iNRG runs. In Fig. 6(c), T_{FL} decreases by roughly one order of magnitude per iNRG run.

When the dependence of T_{FL} on the model parameters is not known analytically, a more general bisection method can instead be used to locate the critical point, provided the two phases separated by it can be distinguished in different iNRG runs. For example, in the 2CKM, the critical point J_2^c separates Kondo strong coupling phases where the impurity spin is ultimately fully screened by either lead $\alpha = 1$ or 2 (depending on the sign of $J_2 - J_2^c$). These phases can be distinguished by physical observables, e.g., the t matrix for channel α, since $t_{\alpha=2}(0) = 1$ and $t_{\alpha=1}(0) = 0$ when $J_2 > J_2^c$. In practice, a simpler and more direct way to distinguish the two phases involves comparing their NRG fixed point energy level structures, which are indexed differently.

The bisection method also involves multiple iNRG runs: each new run uses a value J_2 that is an average of two previous J_2 values (one in each phase) lying closest to each other. T_{FL} does not need to be calculated explicitly here. This protocol also locates the critical point exponentially rapidly (although utilizing information about the functional dependence of T_{FL}, where available, is the optimal strategy).

Finally, we note that the precise value of J_2^c in iNRG depends on the discretization details. However, the critical ratio J_2^c/J_1 is generally found to deviate from its exact (undiscretized) value of 1 by about 1% [see the inset of Fig. 6(d)]. We also find that J_2^c/J_1 converges to a specific value on increasing E_{trunc}, and is essentially invariant for $E_{\mathrm{trunc}} > 7$. This indicates that the critical value of J_2^c determined by the above tuning protocol in iNRG is the true (converged) value *for the asymmetrically discretized model.*

V. CONCLUSION

In this paper, we compared two methods for treating multiband quantum impurity problems with NRG: sNRG exploiting model symmetries [26], and iNRG exploiting symmetry-breaking [23]. Our analysis of the NRG discarded weight [27] and the error in certain calculated physical quantities demonstrates that sNRG and iNRG are of comparable accuracy when the same discretization parameter Λ is used, and when the same number of states are kept on average at each iteration. iNRG therefore constitutes a more fine-grained RG scheme, in which intermediate state-space truncations do not adversely affect convergence or accuracy.

For models that possess high intrinsic symmetries, sNRG is a highly efficient tool for treating multiband quantum impurity problems, because full use can be made of the symmetries. But in models with lower symmetries, sNRG quickly becomes inefficient, and in practice unusable, when more than two spinful conduction electron channels are involved.

We find that iNRG is much more efficient than sNRG for treating a given model with equivalent settings. This is the appropriate comparison for systems where bare model flavor symmetries are already broken. Such a scenario naturally arises on inclusion of a magnetic field, potential scattering, channel anisotropies, and in the *vicinity* of high-symmetry critical points. In these cases, iNRG has the clear advantage.

For high-symmetry models where sNRG can exploit larger symmetries than iNRG, the "best" sNRG and iNRG calculations are found to be of roughly comparable efficiency. In this case, iNRG can be regarded as a viable and technically simple alternative to sNRG. However, *optimal* efficiency can often be obtained by *combining* features of sNRG and iNRG to interleave the Wilson chains for some electronic flavors, while retaining and exploiting other symmetries.

The results of this paper suggest that iNRG could find powerful application as an impurity solver for multiband DMFT. For example, Hubbard models of transition metal oxides with partially filled d orbitals, ruthenates, or iron pnictide and chalcogenide high-temperature superconductors map within DMFT to effective multichannel impurity problems that could be solved accurately using iNRG. In the context of simulating real strongly correlated materials, channel symmetries are generally broken (for example, due to crystal field splitting). Our analysis indicates the feasibility of studying such channel-asymmetric models for three effective channels, and further suggests that 4- and even 5-channel problems could be tackled using iNRG in the future.

We conclude that iNRG is a competitive and versatile alternative to sNRG, even for high-symmetry models. When large symmetries are not available, iNRG is far more efficient that sNRG. Moreover, iNRG provides a way forward for complex models with lower symmetries that are beyond the reach of sNRG, opening up possibilities for new applications of NRG as an impurity solver.

ACKNOWLEDGMENTS

K.M.S., A.W., and J.v.D. were supported by the DFG through SFB-TR12, SFB631, WE4819/1-1, WE4819/2-1, and the Cluster of Excellence *NanoSystems Initiative Munich*. AKM acknowledges funding from the D-ITP consortium, a program of the Netherlands Organisation for Scientific Research (NWO) that is funded by the Dutch Ministry of Education, Culture and Science (OCW).

APPENDIX A: CHOICE OF TRUNCATION ENERGY IN iNRG

In this Appendix, we provide a heuristic justification of the choice of truncation energy $E_{\mathrm{trunc}}^{\mathrm{iNRG}}$ proposed in Eq. (15). In iNRG, the subsites $\tilde{n} = (n,\nu)$ of supersite n are added one by one, each followed by a truncation with a different absolute truncation energy, $\mathrm{E}_{\text{abs-trunc}}^{\mathrm{iNRG}} = E_{\mathrm{trunc}}^{\mathrm{iNRG}} \tilde{\omega}_{(n,\nu)}$. The geometric average of these truncation energies over the supershell is

$$\left\langle E_{\mathrm{abs-trunc}}^{\mathrm{iNRG}} \right\rangle_n^{\mathrm{geom}} = E_{\mathrm{trunc}}^{\mathrm{iNRG}} \left(\prod_{\nu=1}^{m} \tilde{\omega}_{(n,\nu)} \right)^{1/m}. \qquad \text{(A1)}$$

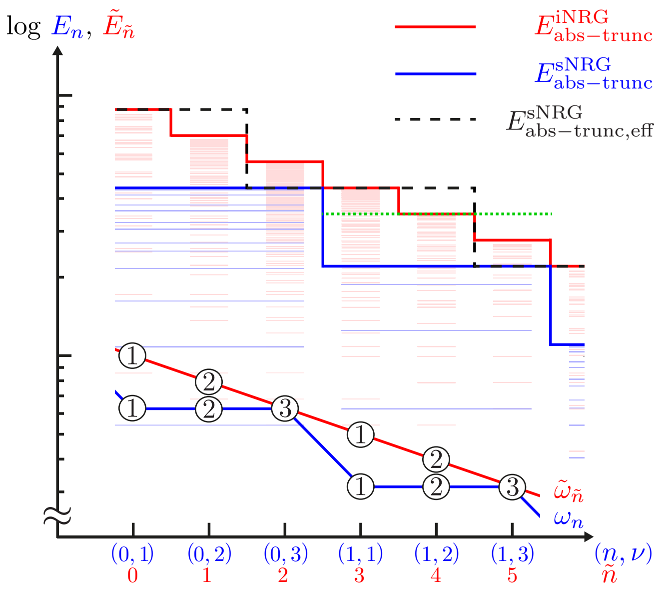

FIG. 7. Schematic depiction of the sNRG (blue) and iNRG (red) truncation schemes used here, illustrated for a model with $m = 3$ flavors. The vertical axis corresponds to absolute energies on a logarithmic scale, while the Wilson (sub)shell index is given on the horizontal axis. The lower part of the sketch depicts the evolution of the characteristic energies ω_n and $\tilde{\omega}_{\tilde{n}}$ for sNRG and iNRG. Thin faint blue and red lines depict the excitation eigenenergies (relative to the ground state energy) of sNRG supershells or iNRG subshells. In sNRG, all three subsites comprising the supersite for that iteration are added at once (there is no intermediate truncation), while in iNRG the subsites are added separately, and truncation occurs at each step. The absolute truncation energies $\mathrm{E}^{\rm sNRG}_{\rm abs\text{-}trunc}$ and $\mathrm{E}^{\rm iNRG}_{\rm abs\text{-}trunc}$ therefore form two different staircases, depicted as the thick blue and red lines, respectively (the step width for sNRG is m times longer than that of iNRG). States with higher energies are discarded. The truncation pattern of sNRG, when viewed from the perspective of iNRG, amounts to employing the effective truncation energy $\mathrm{E}^{\rm sNRG}_{\rm abs\text{-}trunc,eff}$, shown as the black dashed line: by using a high truncation threshold (that of the previous iteration, $E^{\rm sNRG}_{\rm trunc} \times \omega_{n-1}$) for the first $m-1$ subsites, and then dropping to $E^{\rm sNRG}_{\rm trunc} \times \omega_n$ only for the last subsite, all states are effectively kept until the supersite is complete. Viewed from this iNRG perspective, the truncation energies of iNRG and sNRG are the same on average (green dotted line for supersite $n = 1$) and the areas under the red solid, black dashed, and green dotted lines are the same, provided $E^{\rm sNRG}_{\rm trunc}$ and $E^{\rm iNRG}_{\rm trunc}$ are related via Eq. (15).

In sNRG, by contrast, all m subsites of supersite n are added as one unit, followed by truncation at the absolute truncation energy $\mathrm{E}^{\rm sNRG}_{\rm abs\text{-}trunc} = E^{\rm sNRG}_{\rm trunc}\omega_n$. The thick red and blue lines in Fig. 7 show the resulting evolution of the absolute truncation energies in iNRG and sNRG with NRG iteration number, respectively. The characteristic energies $\tilde{\omega}_{\tilde{n}}$ and ω_n are shown as the circles in the lower part of the figure.

To meaningfully compare sNRG and iNRG, it is instructive to view the truncation profile of sNRG within the framework of iNRG. One can think of sNRG as an effective iNRG calculation, in which subsites are added separately, but the effective truncation threshold $\mathrm{E}^{\rm sNRG}_{\rm abs\text{-}trunc,eff}$ for the first $m-1$ subsites is high enough so that all states are kept. This is guaranteed by using the absolute truncation energy of the previous iteration, $\mathrm{E}^{\rm sNRG}_{\rm trunc} \times \omega_{n-1}$. Only when the supersite is complete after adding the last subsite with $\nu = m$, the effective absolute trucation energy is reduced to induce the necessary truncation $\mathrm{E}^{\rm sNRG}_{\rm trunc} \times \omega_n$. Overall, the effective truncation energy in sNRG is subsite-dependent: specifically, within supersite n, we have $\mathrm{E}^{\rm sNRG}_{\rm abs\text{-}trunc,eff} = E^{\rm sNRG}_{\rm trunc} \times \omega_{n-1+\delta_{\nu m}}$. This is shown as the black dashed line in Fig. 7. The geometric average of the effective sNRG truncation energies is

$$\left\langle E^{\rm sNRG}_{\rm abs\text{-}trunc,eff}\right\rangle^{\rm geom}_n = E^{\rm sNRG}_{\rm trunc}\left(\omega_n \prod_{\nu=1}^{m-1}\omega_{n-1}\right)^{1/m}. \qquad \text{(A2)}$$

By demanding that the average truncation energies Eqs. (A1) and (A2) are the same (illustrated by the green dotted line in Fig. 7 for iteration $n = 1$), we obtain the relation between $E^{\rm iNRG}_{\rm trunc}$ and $E^{\rm sNRG}_{\rm trunc}$ announced in Eq. (15).

Finally, we comment that, given a specific number of flavors m, the choice of Eq. (15) implies that the area under the lines $\mathrm{E}^{\rm iNRG}_{\rm abs\text{-}trunc}$ (red) and $\mathrm{E}^{\rm sNRG}_{\rm abs\text{-}trunc,eff}$ (black dashed) is the same for each supersite n and (as examplified for $n = 1$ in Fig. 7) corresponds to the area under the green dotted line.

The important consequence of effectively using 'same' absolute truncation energies on average is that the number of kept states turns out to be the same on average for iNRG and sNRG. Nevertheless, similar to even-odd effects in the number of states of sNRG, subshell-dependent variations of $N_{\rm K}$ occur in iNRG (see Fig. 3).

APPENDIX B: DISCARDED WEIGHT BASED ON ENERGY EIGENSTATES

In this Appendix, we describe how to quantify the contributions of highlying *energy eigenstates* to reduced density matrices, rather than evaluating the eigenspectrum of the reduced density matrices as in Ref. [27]. We do this by analyzing the diagonal weights of $\hat{\rho}$, i.e., the diagonal elements of the reduced density matrix in the *energy* eigenbasis $|s\rangle_{\rm K}$ within the kept sector, $\rho_s = {}_{\rm K}\langle s|\hat{\rho}|s\rangle_{\rm K}$. Hence we employ a strategy analogous to that of Ref. [27], but here we use the energy eigenbasis (cf. Fig. 3 of Ref. [27] and Fig. 8) rather than the eigenbasis of the reduced density matrices (cf. Fig. 4 of Ref. [27]) to estimate the discarded weight. This leads to a slightly different definition of the discarded weight, as described below.

Due to the energy scale separation in NRG, the diagonal weights of the reduced density matrices decrease exponentially when plotted versus their corresponding rescaled eigenenergies (cf. colored dots in Fig. 8). The same is true for the integrated weight distribution [cf. Eq. (18) of Ref. [27] and black solid line in Fig. 8], which as such constitutes an upper bound for the weights, and scales as $\rho(E) \approx \kappa \mathrm{e}^{-\kappa E}$ (normalized such that $\int_0^\infty \rho(E)\,dE = 1$). This exponential decay shows that the contribution of an NRG state with rescaled energy E to the properties of subsequent shells decreases exponentially with E. This justifies the strategy in NRG to keep track of these contributions only up to a threshold energy of $E_{\rm trunc}$. Moreover, by extrapolating the exponential form to energies beyond $E_{\rm trunc}$, the sum of weights associated with all discarded high energy states with $E > E_{\rm trunc}$ can be estimated. We therefore define the total discarded weight by

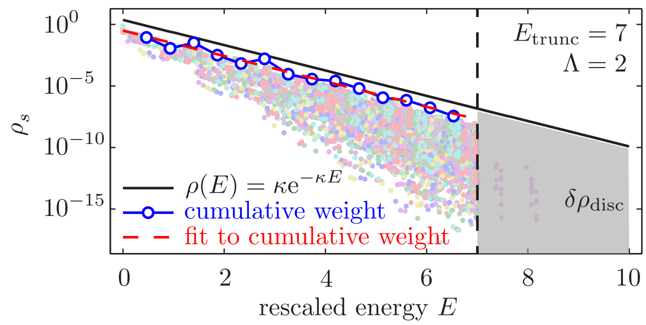

FIG. 8. Estimating the discarded weight, $\delta\rho_{\rm disc}$, of a single NRG run. Colored dots show the diagonal weights of the reduced density matrices in the energy eigenbasis of NRG. Different colors represent the weights for different NRG iterations. We calculate and plot the cumulative weights (blue open circles) using 16 bins in the energy window $[0, E_{\rm trunc}]$. The truncation energy $E_{\rm trunc} = 7$ is indicated by the vertical black dashed line. The red dashed line is an exponential fit to the cumulative weights; its slope gives κ as defined in Eq. (B1). The black line shows the normalized integrated weight distribution $\rho(E) = \kappa e^{-\kappa E}$, extrapolated to energies $E > E_{\rm trunc}$. The shaded grey area under this black line then serves as estimate for the discarded weight: $\delta\rho_{\rm disc} = e^{-\kappa E_{\rm trunc}}$. This example is well-converged, with $\kappa = 2.37$ yielding $\delta\rho_{\rm disc} = 6.23 \times 10^{-8}$.

the following integral (represented by the shaded grey area in Fig. 8):

$$\delta\rho_{\rm disc} = \int_{E_{\rm trunc}}^{\infty} \rho(E)\, dE = e^{-\kappa E_{\rm trunc}} . \qquad \text{(B1)}$$

In practice, we obtain $\delta\rho_{\rm disc}$ numerically as follows. First, a cumulative histogram is constructed of the discrete weights ρ_s for $E < E_{\rm trunc}$ over all NRG iterations, using coarse-grained energy bins (e.g., keeping 16 bins in the energy window $[0, E_{\rm trunc}]$). This histogram represents $\rho(E)$. A linear fit to its shape on a semilogarithmic scale then yields κ, which in turn gives $\delta\rho_{\rm disc}$, via Eq. (B1) . Since $\delta\rho_{\rm disc}$ depends only on the dimensionless quantity $\kappa E_{\rm trunc}$, the result is independent of the choice of energy unit for $E_{\rm trunc}$.

By examining the decay of the discarded weight $\delta\rho_{\rm disc}$ with increasing $E_{\rm trunc}$, and observing the corresponding convergence of physical quantities, we have found that calculations can be considered converged when $\delta\rho_{\rm disc} < 10^{-6}$. This convergence criterion has been determined to ensure that further increasing $E_{\rm trunc}$ does not qualitatively change the results [see, e.g., Figs. 2(j)–2(o)]. We note that the numerical value of this threshold is about the square-root of and thus considerably larger than that reported in Ref. [27], which was obtained using the alternative definition of discarded weight in terms of the eigenspectrum of reduced density matrices.

An important advantage of defining the discarded weight in terms of the energy eigenbasis is that $\delta\rho_{\rm disc}$, evaluated at fixed $E_{\rm trunc}$, is rather insensitive to changing the discretization parameter Λ (we verified this explicitly over a range of Λ typically used in NRG, $1.7 \lesssim \Lambda \lesssim 7$). We found that $E_{\rm trunc} \gtrsim 7$ generally suffices to obtain well-converged results for physical quantities. In contrast, the discarded weight defined in terms of density matrix eigenvalues [27] turns out to show a much more pronounced dependence on Λ at fixed $E_{\rm trunc}$, which would be inconvenient for the present purposes.

[1] A. C. Hewson, *The Kondo Problem to Heavy Fermions* (Cambridge University Press, Cambridge, 1993).
[2] J. Kondo, Prog. Theor. Phys. **32**, 37 (1964).
[3] K. G. Wilson, Rev. Mod. Phys. **47**, 773 (1975).
[4] H. R. Krishnamurthy, J. W. Wilkins, and K. G. Wilson, Phys. Rev. B **21**, 1003 (1980).
[5] R. Bulla, T. Costi, and T. Pruschke, Rev. Mod. Phys. **80**, 395 (2008).
[6] T. A. Costi, L. Bergqvist, A. Weichselbaum, J. von Delft, T. Micklitz, A. Rosch, P. Mavropoulos, P. H. Dederichs, F. Mallet, L. Saminadayar, and C. Bäuerle, Phys. Rev. Lett. **102**, 056802 (2009).
[7] M. Hanl, A. Weichselbaum, T. A. Costi, F. Mallet, L. Saminadayar, C. Bäuerle, and J. von Delft, Phys. Rev. B **88**, 075146 (2013).
[8] B. A. Jones, C. M. Varma, and J. W. Wilkins, Phys. Rev. Lett. **61**, 125 (1988); B. A. Jones, Physica B: Condens. Matter **171**, 53 (1991).
[9] A. K. Mitchell, P. G. Derry, and D. E. Logan, Phys. Rev. B **91**, 235127 (2015).
[10] J. Bork, Y. hui Zhang, L. Diekhöner, L. Borda, P. Simon, J. Kroha, P. Wahl, and K. Kern, Nat. Phys. **7**, 901 (2011).
[11] A. Schwabe, M. Hänsel, M. Potthoff, and A. K. Mitchell, Phys. Rev. B **92**, 155104 (2015).
[12] P. Jarillo-Herrero, J. Kong, H. S. J. van der Zant, C. Dekker, L. P. Kouwenhoven, and S. D. Franceschi, Nature **434**, 484 (2005).
[13] S. J. Chorley, M. R. Galpin, F. W. Jayatilaka, C. G. Smith, D. E. Logan, and M. R. Buitelaar, Phys. Rev. Lett. **109**, 156804 (2012).
[14] M. Pustilnik, L. Borda, L. I. Glazman, and J. von Delft, Phys. Rev. B **69**, 115316 (2004).
[15] A. K. Mitchell and D. E. Logan, Phys. Rev. B **81**, 075126 (2010).
[16] A. K. Mitchell, D. E. Logan, and H. R. Krishnamurthy, Phys. Rev. B **84**, 035119 (2011).
[17] B. Béri and N. R. Cooper, Phys. Rev. Lett. **109**, 156803 (2012).
[18] M. R. Galpin, A. K. Mitchell, J. Temaismithi, D. E. Logan, B. Beri, and N. R. Cooper, Phys. Rev. B **89**, 045143 (2014).
[19] A. Georges, G. Kotliar, W. Krauth, and M. J. Rozenberg, Rev. Mod. Phys. **68**, 13 (1996).
[20] T. Pruschke and R. Bulla, Eur. Phys. J. B **44**, 217 (2005).
[21] K. M. Stadler, Z. P. Yin, J. von Delft, G. Kotliar, and A. Weichselbaum, Phys. Rev. Lett. **115**, 136401 (2015).
[22] M. H. Hettler, M. Mukherjee, M. Jarrell, and H. R. Krishnamurthy, Phys. Rev. B **61**, 12739 (2000).
[23] A. K. Mitchell, M. R. Galpin, S. Wilson-Fletcher, D. E. Logan, and R. Bulla, Phys. Rev. B **89**, 121105(R) (2014).
[24] A. I. Tóth and G. Zaránd, Phys. Rev. B **78**, 165130 (2008).
[25] W. Hofstetter, Phys. Rev. Lett. **85**, 1508 (2000).

[26] A. Weichselbaum, Ann. Phys. **327**, 2972 (2012).
[27] A. Weichselbaum, Phys. Rev. B **84**, 125130 (2011).
[28] L. N. Oliveira, V. L. Libero, H. O. Frota, and M. Yoshida, Physica B: Condensed Matter **171**, 61 (1991).
[29] W. C. Oliveira and L. N. Oliveira, Phys. Rev. B **49**, 11986 (1994).
[30] R. Zitko and T. Pruschke, Phys. Rev. B **79**, 085106 (2009).
[31] A. Weichselbaum and J. von Delft, Phys. Rev. Lett. **99**, 076402 (2007).
[32] F. B. Anders and A. Schiller, Phys. Rev. Lett. **95**, 196801 (2005); Phys. Rev. B **74**, 245113 (2006).
[33] P. Nozières and A. Blandin, J. Phys. (Paris) **41**, 193 (1980).
[34] I. Affleck, A. W. W. Ludwig, H.-B. Pang, and D. L. Cox, Phys. Rev. B **45**, 7918 (1992).
[35] E. Sela, A. K. Mitchell, and L. Fritz, Phys. Rev. Lett. **106**, 147202 (2011); A. K. Mitchell and E. Sela, Phys. Rev. B **85**, 235127 (2012).
[36] M. Hanl, A. Weichselbaum, J. von Delft, and M. Kiselev, Phys. Rev. B **89**, 195131 (2014).
[37] I. Affleck and A. W. W. Ludwig, Phys. Rev. B **48**, 7297 (1993).